ISSN 0915-633

NATIONAL INSTITUTE FOR FUSION SCIENCE

Macro-EM Particle Simulation Method and A Study of Collisionless Magnetic Reconnection

M. Tanaka

(Received - Oct. 18, 1994)

NIFS-316 Nov. 1994

RESEARCH REPORT
NIFS Series

NAGOYA, JAPAN

Macro-EM Particle Simulation Method and A Study of Collisionless Magnetic Reconnection

Motohiko Tanaka

National Institute for Fusion Science
Furoh-cho, Nagoya 464-01, Japan

Abstract

A multi-dimensional electromagnetic particle simulation method which is suitable for studying low-frequency plasma phenomena is described in the first part. Its application to collisionless magnetic reconnection is shown in the second part. The present particle code efficiently deals with nonlinear kinetic processes wherein ions and electrons play their roles, since the code is implemented using the Maxwell equations and the Newton-Lorentz equations. The drift-kinetic equations are used optionally. A simulation of collisionless reconnection shows that the toroidal electric field which directly relates to reconnection is generated naturally in the kinetic study, and that a thin dissipation region is formed whose width is a few electron skin depth. Thus, collisionless reconnection is considered to proceed under the electron inertia.

Keywords: implicit time-integration, particle simulation,
plasma physics, magnetic reconnection

1. Introduction

In space and fusion plasma studies, there is a wide class of low-frequency, electromagnetic phenomena where the ions and electrons play significant roles in wave generation and damping, plasma instability, and particle transport along the magnetic field. Well-known examples that belong to this "meso-scale" category located between the micro and macro (magnetohydrodynamic)-scale regimes are the kinetic Alfven wave[1], the toroidicity-induced Alfven eigenmode[2], the m=1 tearing mode[3,4], and collisionless magnetic reconnection[5]. In these phenomena, either the polarization drift or finite Larmor radius of the ions, Landau damping or finite inertia of the electrons are indispensable elements to support the physical processes. Simulations of the kinetic Alfven wave[6] and collisionless magnetic reconnection[7] have been performed in the recent years using the implicit particle scheme.

Since the aforementioned phenomena frequently develops into highly nonlinear stages, the numerical simulation is considered to be quite a reliable, self-consistent approach in theoretical studies. However, it was fairly difficult until recently to deal with these low-frequency, kinetic processes by the conventional explicit particle scheme[8] or the magnetohydrodynamic (MHD) fluid code. This was particularly due to disparity of the time-and-space scales of the phenomena that we are actually interested in and the micro-scales that the particle scheme has to resolve. Starting at the beginning of 1980's, various types of advanced particle simulation schemes were developed to remove difficulties of this disparity. These are the implicit particle simulation techniques[9–15], and the gyrokinetic approach[16].

The implicit particle schemes make only loose assumptions on the frequency, wavenumber and amplitude of the electromagnetic field. Thus, the methods are best applied to nonlinear, low-frequency kinetic phenomena such as collisionless magnetic reconnection and edge plasma turbulence. Among the implicit particle schemes, the moment-implicit method[9–11] and the direct-implicit method[12,13] were developed in early 1980's, and the closely-coupled implicit method ("macro-particle" code)[14,15] in the middle of the decade. By contrast, the gyrokinetic scheme makes extensive assumptions on the

electromagnetic field to be treated. Owing to this ordering, the gyrokinetic scheme is accurate and efficient when it is applied to studies of weakly nonlinear, low-frequency plasma phenomena such as transport in magnetic fusion devices. Another class of the particle scheme, the hybrid-particle code with massless electrons[17] is applicable only when the electron kinetic effects are ignorable.

The moment-implicit method[9,10] is a natural extension of the fluid concept to the kinetic regime. It derives implicit moment equations to calculate the future electromagnetic field with the particle velocity moments as the source terms. The algorithm is numerically stable, but, until recent development of the CELEST1D algorithm[11], the scheme was prevented from exploiting the possibility of using very large time steps by inability to solve the field equations, although the time step with the VENUS code[10] was larger than with explicit schemes.

The direct-implicit method[12,13] constructs a high-accuracy low-pass time filter by combining the electric acceleration of a few time levels to control numerical damping of high-frequency waves in the plasma. The future current density is directly predicted by pushing particles and later corrected implicitly in the field equations. In contrast to its mathematical high accuracy, however, its numerical stability is actually supported by additional smoothing in the time domain.

The closely-coupled implicit method[14,15] uses fully time-implicit, kinetic field equations to determine the electromagnetic field. These equations are derived by combining the Maxwell equations and the equations of motion. The current and charge densities are expressed in terms of the present and future electromagnetic fields to make a closure of the equations. The time-decentering technique is introduced, but the equations do not need additional prediction of the future fields. The algorithm is thus stable for large time-and-space scales without an extra smoothing in time.

Important features of the "macro-particle code" - HIDEN[18], which is based on the above closely-coupled field-particle equations, are listed in Table I. The basic feature is that the low-frequency electromagnetic waves with $\omega_0 \Delta t \ll 1$ are properly reproduced, where ω_0 is their characteristic frequency and Δt is a time step of the simulation. Since the ions and electrons are treated as charged particles, various particle resonance

and orbit effects are incorporated in the natural fashion. Moreover, the method works numerically well both in the linear and nonlinear stages of the plasma phenomena by virtue of the fully-implicit field equations. These features make the closely-coupled implicit method suitable for studying nonlinear, kinetic plasma processes in large time-and-space scales.

The outline of this article will be the following. In Section 2, the algorithm of the closely-coupled implicit method will be described for both magnetized and unmagnetized cases. Numerical methods and techniques including matrix inversion required in the code implementation will be shown in Section 3. A simulation of collisionless reconnection in a unmagnetized plasma will be presented in Section 4. Finally, Section 5 will conclude the article with a summary and future prospects of the implicit simulation method.

2. Algorithm for the Low-Frequency Kinetic Plasma Simulations

2.1 Equations of the Field and Particles

The present implicit particle scheme adopts the Newton-Lorentz equations of motion and the Maxwell equations to describe an evolution of the kinetic plasmas[14,15], like the standard electromagnetic particle simulation scheme. However, to realize a large time-and-space scale simulation, a slightly backward time-decentering technique is introduced. The Maxwell equations with time level suffices are written

$$\frac{1}{c}\left(\frac{\partial \mathbf{E}}{\partial t}\right)^{n+1/2} = \nabla \times \mathbf{B}^{n+\alpha} - \frac{4\pi}{c}\mathbf{J}^{n+\alpha}, \tag{1}$$

$$\frac{1}{c}\left(\frac{\partial \mathbf{B}}{\partial t}\right)^{n+1/2} = -\nabla \times \mathbf{E}^{n+\alpha}, \tag{2}$$

$$\nabla \cdot \mathbf{E}^{n+1} = 4\pi\rho^{n+1}, \tag{3}$$

$$\nabla \cdot \mathbf{B}^{n+1} = 0. \tag{4}$$

Here, $\mathbf{E}$ and $\mathbf{B}$ are the electric and magnetic fields, respectively, c is the speed of light, and α is a decentering (implicitness) parameter to be specified later. The current density $\mathbf{J}$ and the charge density ρ are implicit quantities, which are not the simple sums of particle quantities but are expressed in terms of the present and unknown future electromagnetic fields.

To describe the particle motion, either the Newton-Lorentz equations or the drift-kinetic equations are used. An advantage of the Newton-Lorentz equations is inclusion of the full particle dynamics under the constraint of $|\omega_{cj}|\Delta t < 1$, where $\omega_{cj} = e_j B/m_j c$ is the cyclotron frequency of the j-th particle. These equations must be used to simulate a plasma with magnetic-null points. The drift-kinetic equations allow us to use large time steps and are suitable for magnetized plasmas. These equations are optionally used for the magnetized electrons.

The Newton-Lorentz equations of motion with the time level suffices are written

$$\left(\frac{d\mathbf{v}_j}{dt}\right)^{n+1/2} = \left(\frac{e_j}{m_j}\right)\left[\mathbf{E}^{n+\alpha}(\mathbf{x}_j) + (\mathbf{v}_j^{n+1/2}/c) \times \mathbf{B}^{n+\alpha}(\mathbf{x}_j)\right], \tag{5}$$

$$\left(\frac{d\mathbf{x}_j}{dt}\right)^{n+1/2} = \mathbf{v}_j^{n+1/2}, \tag{6}$$

Solving Eq.(12) for the future velocity $\mathbf{v}_j^{n+1}$ using the linear interpolation $\mathbf{v}^{n+1/2} = \frac{1}{2}(\mathbf{v}^n + \mathbf{v}^{n+1})$ yields

$$\begin{aligned}\mathbf{v}_j^{n+1} &= \mathbf{v}_j^n + \Delta t \frac{e_j}{m_j} \left\{ \left(\tilde{\mathbf{E}}^{n+\alpha} + \frac{\mathbf{v}_j^n}{c} \times \tilde{\mathbf{B}}^{n+\alpha} \right) + \Theta^2 \tilde{\mathbf{E}}_{\|}^{n+\alpha} \right. \\ &\quad \left. + \Theta \left(\tilde{\mathbf{E}}^{n+\alpha} + \frac{\mathbf{v}_j^n}{c} \times \tilde{\mathbf{B}}^{n+\alpha} \right) \times \tilde{\mathbf{b}}^{n+\alpha} \right\} / (1 + \Theta^2), \qquad (14) \\ \mathbf{x}_j^{n+1} &= \mathbf{x}_j^n + \Delta t \; \mathbf{v}_j^{n+1/2}, \qquad (15)\end{aligned}$$

where $\tilde{\mathbf{E}}_{\|}^{n+\alpha} = (\tilde{\mathbf{E}}^{n+\alpha} \cdot \tilde{\mathbf{b}}^{n+\alpha}) \, \tilde{\mathbf{b}}^{n+\alpha}$, and $\Theta(\mathbf{x}) = \frac{1}{2}\Delta t (e_j/m_j c) |\tilde{\mathbf{B}}|^{n+\alpha}$. The first term in the right-hand side of Eq.(14), $\mathbf{v}_j^n$, which is independent of the future magnetic field $\mathbf{B}^{n+\alpha}$, has been purposely separated out. In the $|\Theta| \gg 1$ limit corresponding to the guiding-center approximation, the first-order terms of Eq.(14) are

$$\mathbf{v}_j^{n+1} \cong \mathbf{v}_j^n + \Delta t \frac{e_j}{m_j} \left\{ \tilde{\mathbf{E}}_{\|}^{n+\alpha} + \frac{1}{\Theta} \left(\tilde{\mathbf{E}}^{n+\alpha} + \frac{\mathbf{v}_j^n}{c} \times \tilde{\mathbf{B}}^{n+\alpha} \right) \times \tilde{\mathbf{b}}^{n+\alpha} \right\}. \qquad (16)$$

Decomposition of the parallel and perpendicular components in terms of the local magnetic field direction $\mathbf{b}^{n+\alpha}$ yields

$$\begin{aligned}\mathbf{v}_{\perp j}^{n+1} &\cong c \tilde{\mathbf{E}}^{n+\alpha} \times \tilde{\mathbf{b}}^{n+\alpha} / B^{n+\alpha}, \qquad (17) \\ v_{\| j}^{n+1} &\cong v_{\| j}^n + \Delta t \frac{e_j}{m_j} (\tilde{\mathbf{E}}^{n+\alpha} \cdot \tilde{\mathbf{b}}^{n+\alpha}). \qquad (18)\end{aligned}$$

These are obviously the leading terms of the drift-kinetic equations Eqs.(8),(9). The drift-kinetic equations are similarly discretized in time and are written as

$$\begin{aligned}v_{\| j}^{n+1} &= v_{\| j}^n + \Delta t \left(\left(\frac{e_j}{m_j} \right) \tilde{E}_{\|}^{n+\alpha} - \left(\frac{\mu_j}{m_j} \right) \frac{\partial}{\partial x_{\|}} \tilde{B}^{n+\alpha} \right), \qquad (19) \\ \mathbf{x}_j^{n+1} &= \mathbf{x}_j^n + \Delta t \left\{ \mathbf{v}_{\| j}^{n+1/2} + \mathbf{v}_{\perp j}^{n+\alpha}(\bar{\mathbf{x}}_j^{n+1/2}) \right\}. \qquad (20)\end{aligned}$$

The perpendicular velocity is a function of the future electromagnetic field as specified by Eq.(9), and the direction of the parallel velocity is defined by Eq.(11).

Also, the Maxwell equations are discretized with respect to time and are written

$$\begin{aligned}\mathbf{E}^{n+1} - \mathbf{E}^n &= c\Delta t \nabla \times \mathbf{B}^{n+\alpha} - 4\pi \Delta t \; \mathbf{J}^{n+\alpha}, \qquad (21) \\ \mathbf{B}^{n+1} - \mathbf{B}^n &= -c\Delta t \nabla \times \mathbf{E}^{n+\alpha}. \qquad (22)\end{aligned}$$

To relax the Courant condition, we eliminate $\mathbf{B}^{n+1}$ from Eqs.(21),(22) to obtain an implicit equation of $\mathbf{E}^{n+1}$. If we use for $\mathbf{E}^{n+\alpha}$ the linear interpolation to the non-integer time level

$$\mathbf{E}^{n+\alpha} \;=\; \alpha\mathbf{E}^{n+1} \;+\; (1-\alpha)\mathbf{E}^{n}, \tag{23}$$

and a similar formula for $\mathbf{B}^{n+\alpha}$, we obtain the equation of the future electric field $\mathbf{E}^{n+1}$,

$$\begin{aligned}[\,1+(\alpha c\Delta t)^2\nabla\times\nabla\times\,]\,\mathbf{E}^{n+1} \;=\; &[\,1-\alpha(1-\alpha)(c\Delta t)^2\nabla\times\nabla\times]\,\mathbf{E}^{n}\\ &+\,c\Delta t\nabla\times\mathbf{B}^{n}\;-\;4\pi\Delta t\;\mathbf{J}^{n+\alpha}.\end{aligned} \tag{24}$$

The functional form of the current density in the right-hand side of the equation will be specified in Section 2.3. The future magnetic field is determined by Eq.(22) after $\mathbf{E}^{n+1}$ has been solved.

Mathematically, Eq.(24) is nearly decomposed into the magnetostatic component $\nabla\times\mathbf{B}^{n+\alpha}=(4\pi/c)\;\mathbf{J}_T^{n+\alpha}$ and the electrostatic component $\mathbf{E}_L^{n+1}=\mathbf{E}_L^{n}-4\pi\Delta t\;\mathbf{J}_L^{n+\alpha}$ if $(c\Delta t/\lambda)^2\gg 1$ ($\nabla\times\approx 1/\lambda$) holds, where (T) and (L) denote the transverse (divergence-free) and longitudinal (curl-free) parts, respectively. The unity terms in the square brackets of Eq.(24) are the major terms of the electrostatic part and cannot be ignored. Despite of apparent simplicity, the decomposed equations (Darwin algorithm)[17] are hardly used in the real space solution because a complete separation of the transverse current $\mathbf{J}_T$ ($\nabla\cdot\mathbf{J}_T=0$) from the longitudinal current $\mathbf{J}_L$ ($\nabla\times\mathbf{J}_L=0$) is almost impossible.

Finally, it must be noted that the electrostatic equation which is equivalently transformed by Eq.(3) into

$$(\rho^{n+1}-\rho^{n})/\Delta t \;+\; \nabla\cdot\mathbf{J}_L^{n+\alpha}=0, \tag{25}$$

disagrees with the continuity equation. This discrepancy contained in the solution to Eq.(24) must be corrected later by using the Poisson equation $\nabla\cdot\mathbf{E}^{n+1}=4\pi\rho^{n+1}$ (Section 2.3(b)).

2.3 The Closely-Coupled Field-Particle (CCFP) Equations

(a) Time-Implicit Equations for the Electromagnetic Field

In order to make a closure of Eq.(24), the current density must be specified. The method of predicting the future current density constitutes the key of the implicit particle schemes. In the closely-coupled implicit method, the current density is expressed plainly in terms of the future electromagnetic field with aid of the equations of motion. The current density in the electron drift-kinetic code consists of totally different ion and electron parts, as given by

$$\begin{aligned}
\mathbf{J}^{n+\alpha}(\mathbf{x}) &= \sum_j e_j \mathbf{v}_j^{n+\alpha} S(\mathbf{x}-\bar{\mathbf{x}}_j^{n+\alpha}) \\
&= \sum_{j=i} e_i \left[\mathbf{v}_j^n + \alpha\Delta t \frac{e_i}{m_i} \left\{\left(\tilde{\mathbf{E}}^{n+\alpha} + \frac{\mathbf{v}_j^n}{c}\times\tilde{\mathbf{B}}^{n+\alpha}\right) + \Theta^2 \tilde{\mathbf{E}}_{\|}^{n+\alpha}\right.\right. \\
&\quad \left.\left. + \Theta\left(\tilde{\mathbf{E}}^{n+\alpha} + \frac{\mathbf{v}_j^n}{c}\times\tilde{\mathbf{B}}^{n+\alpha}\right)\times\tilde{\mathbf{b}}^{n+\alpha}\right\}/(1+\Theta^2)\right] S(\mathbf{x}-\bar{\mathbf{x}}_j^{n+\alpha}) \\
&+ \sum_{j=e}(-e)\left[\left\{v_{\|j}^n + \alpha\Delta t\left(\left(\frac{-e}{m_e}\right)\tilde{E}_{\|}^{n+\alpha} - \left(\frac{\mu_j}{m_e}\right)\frac{\partial}{\partial x_{\|}}\tilde{B}^{n+\alpha}\right)\right\}\tilde{\mathbf{b}}^{n+\alpha}\right. \\
&\quad \left. + \tilde{\mathbf{v}}_{\perp j}^{n+\alpha}(\bar{\mathbf{x}}_j^{n+1/2})\right] S(\mathbf{x}-\bar{\mathbf{x}}_j^{n+\alpha}) \\
&- c\,\nabla\times\sum_{j=e}\mu_j\tilde{\mathbf{b}}^{n+\alpha} S(\mathbf{x}-\bar{\mathbf{x}}_j^{n+\alpha}), \qquad (26)
\end{aligned}$$

where $\sum_{j=i}$ and $\sum_{j=e}$ denote summations over the ion and electron species, respectively. The last term of Eq.(26) accounts for the magnetization current $\mathbf{J}_M = -c\nabla\times(p_\perp^{(e)}\mathbf{b}/B)$ of the electrons under the guiding-center approximation. As before, the electromagnetic field with the tilde is evaluated with the weighting scheme Eq.(13). The basic unknown quantities in the right-hand side of Eq.(26) are $\mathbf{E}^{n+1}$ and $\mathbf{B}^{n+1}$. On the other hand, the current density in the full-kinetics code is given by

$$\begin{aligned}
\mathbf{J}^{n+\alpha}(\mathbf{x}) &= \sum_{j=i,e} e_j \left[\mathbf{v}_j^n + \alpha\Delta t \frac{e_j}{m_j} \left\{\left(\tilde{\mathbf{E}}^{n+\alpha} + \frac{\mathbf{v}_j^n}{c}\times\tilde{\mathbf{B}}^{n+\alpha}\right) + \Theta^2 \tilde{\mathbf{E}}_{\|}^{n+\alpha}\right.\right. \\
&\quad \left.\left. + \Theta\left(\tilde{\mathbf{E}}^{n+\alpha} + \frac{\mathbf{v}_j^n}{c}\times\tilde{\mathbf{B}}^{n+\alpha}\right)\times\tilde{\mathbf{b}}^{n+\alpha}\right\}/(1+\Theta^2)\right] S(\mathbf{x}-\bar{\mathbf{x}}_j^{n+\alpha}). \qquad (27)
\end{aligned}$$

Apparently, the full-kinetics (FK) algorithm is much less complicated than the drift-kinetic (DK) algorithm. In fact, the computational cost per time step with the FK algorithm is about two thirds that of the DK algorithm.

Substitution of the implicitly-expressed current density Eq.(26) or (27) into Eq.(24) yields the matrix equation to determine the future electric field $\mathbf{E}^{n+1}$,

$$A_v\ \mathbf{E}^{n+1} \ = \ \mathbf{S}_p(\mathbf{E}^n, \mathbf{B}^n;\ \mathbf{E}^{n+1}, \mathbf{B}^{n+1}). \tag{28}$$

The matrix A_v on the left-hand side represents a vacuum response which is defined by

$$A_v \ = \ \mathbf{1} \ + \ (\alpha c\Delta t)^2(\nabla\nabla - \mathbf{1}\nabla^2), \tag{29}$$

and the source vector $\mathbf{S}_p$ on the right-hand side is given by

$$\begin{aligned}\mathbf{S}_p \ = \ & [1 - \alpha(1-\alpha)(c\Delta t)^2(\nabla\nabla - \nabla^2)]\ \mathbf{E}^n + c\Delta t\ \nabla \times \mathbf{B}^n \\ & - 4\pi\Delta t\ \{\sum_{j=i} e_i\ [\mathbf{v}_j^n + \alpha\Delta t(e_i/m_i)\left(\tilde{\mathbf{E}}^{n+\alpha} + \frac{\mathbf{v}_j^n}{c} \times \tilde{\mathbf{B}}^{n+\alpha}\right) \\ & \qquad /(1+\Theta^2)]\ S(\mathbf{x} - \bar{\mathbf{x}}_j^{n+\alpha}) \ + \ \cdots\cdots \}.\end{aligned} \tag{30}$$

The symbol $\nabla\nabla$ denotes a dyadic operator and $\mathbf{1}$ the unit tensor. The equations (28)-(30) and (22) constitute a closed set of the Courant-condition-free, implicit equations to determine the future electromagnetic field. These equations are named "closely-coupled field-particle (CCFP) equations" after their nature of close coupling of the fields and particles.

(b) A Correction to the Longitudinal Electric Field

The third and fourth Maxwell equations, Eqs.(3) and (4), are the conditions to determine the initial value of the electromagnetic field, which need not be used mathematically for $t > 0$. However, as demonstrated with Eq.(25), the electrostatic part of Eq.(24) deviates from the charge continuity equation. Moreover, a discreteness of the space grids introduces a small but finite error[19] to the longitudinal (curl-free) part of the area-weighted current density Eq.(26). Hence, a correction to the longitudinal part of the current density must be done in each time step[12–15].

For the correction, the true electric field $\mathbf{E}^{n+1}$ is expressed as a sum of the electric field before the correction $\breve{\mathbf{E}}^{n+1}$ (the solution of Eq.(28)) and a gradient of the scalar function $\delta\varphi$,

$$\mathbf{E}^{n+1} \ = \ \breve{\mathbf{E}}^{n+1} - \nabla\delta\varphi. \tag{31}$$

Substitution of Eq.(31) into the Poisson equation Eq.(3) yields

$$-\nabla^2\delta\varphi \;=\; 4\pi\rho^{n+1} \;-\; \nabla\cdot\breve{\mathbf{E}}^{n+1}. \tag{32}$$

Again, the charge density ρ^{n+1} which is not known at this moment needs to be obtained in an implicit manner to be stable against a large time step. For this purpose, the charge density is Taylor-expanded in terms of a small displacement due to the correction electric field $\nabla\delta\varphi$,

$$\begin{aligned}\rho^{n+1}(\mathbf{x}) \;&=\; \sum_j e_j S(\mathbf{x}-\mathbf{x}_j^{n+1}) \\ &\cong\; \sum_j e_j S(\mathbf{x}-\mathbf{x}_{j(l)}^{n+1}) - \nabla\cdot\left(\sum_j e_j\delta\mathbf{x}_j S(\mathbf{x}-\mathbf{x}_{j(l)}^{n+1})\right),\end{aligned} \tag{33}$$

where the vector identity has been used[20]. The displacement is defined by $\delta\mathbf{x}_j = \mathbf{x}_j^{n+1} - \mathbf{x}_{j(l)}^{n+1}$ with $\mathbf{x}_j^{n+1}$ being the true particle position at $t = t^{n+1}$, and $\mathbf{x}_{j(l)}^{n+1}$ the pivoting position predicted using the known electromagnetic field $\breve{\mathbf{E}}^{n+1}$ and $\mathbf{B}^{n+1}$. The displacement corresponding to the Newton-Lorentz equations Eq.(5),(6) is calculated to be

$$\delta\mathbf{x}_j^{(NL)} \;=\; -\frac{1}{2}\alpha(\Delta t)^2\frac{e_j}{m_j}\{\nabla\delta\varphi + \nabla\delta\varphi\times\Theta\mathbf{b}^{n+\alpha} \;+\; \Theta^2\nabla_\parallel\delta\varphi\}/(1+\Theta^2), \tag{34}$$

where the vector operator is defined by $\nabla_\parallel = \mathbf{b}^{n+\alpha}\,(\mathbf{b}^{n+\alpha}\cdot\nabla)$. Since the final magnetic field is already determined together with $\breve{\mathbf{E}}^{n+1}$ at this stage, the displacement $\delta\mathbf{x}_j$, hence the charge density ρ^{n+1}, is solely a function of $\delta\varphi$. By substituting Eq.(33) into Eq.(32) and shifting the $\delta\varphi$-dependent terms to the left-hand side, we obtain the completely implicit equation to determine $\delta\varphi$ in the electron drift-kinetic code,

$$\begin{aligned}\nabla^2\delta\varphi \;+\; &\frac{1}{2}\alpha(\Delta t)^2\nabla\cdot\Big(\omega_{pi}^2(\mathbf{x})\{\nabla\delta\varphi + \Theta^2\nabla_\parallel\delta\varphi \;+\; \Theta\nabla\delta\varphi\times\mathbf{b}\}/(1+\Theta^2) \\ &+\omega_{pe}^2(\mathbf{x})\,\nabla_\parallel\delta\varphi\Big) \;+\; 4\pi(-e)c\alpha\Delta t\;\nabla\cdot(\nabla\delta\varphi\times(\mathbf{b}/B)\,n_e(\mathbf{x})) \\ =\; &-4\pi\bar{\rho}^{n+1} + \nabla\cdot\breve{\mathbf{E}}^{n+1}.\end{aligned} \tag{35}$$

In the full-kinetics code, we have

$$\begin{aligned}\nabla^2\delta\varphi \;+\; &\frac{1}{2}\alpha(\Delta t)^2\nabla\cdot\left(\sum_{j=i,e}\omega_{pj}^2(\mathbf{x})\{\nabla\delta\varphi + \Theta^2\nabla_\parallel\delta\varphi \;+\; \Theta\nabla\delta\varphi\times\mathbf{b}\}/(1+\Theta^2)\right) \\ =\; &-4\pi\bar{\rho}^{n+1} + \nabla\cdot\breve{\mathbf{E}}^{n+1}.\end{aligned} \tag{36}$$

Here, $\bar{\rho}^{n+1}(\mathbf{x}) = \sum_j e_j S(\mathbf{x}-\mathbf{x}_{j(l)}^{n+1})$ and $\omega_{pj}^2(\mathbf{x}) = 4\pi n_j(\mathbf{x})e_j^2/m_j$. In these equations, the vacuum response $\nabla^2\delta\varphi$ is mostly shielded by the plasma dielectric response, $\frac{1}{2}\alpha(\Delta t)^2\nabla\cdot(\cdots\cdots)$ due to $\omega_{pe}^{(0)}\Delta t \gg 1$.

Before concluding this section, it is emphasized that the full-kinetics code is worthwhile despite of its comparatively small time step $\omega_{ce}\Delta t \cong 1$. First, if the electron cyclotron frequency corresponding to the largest magnetic field is less than the plasma frequency, $\omega_{ce} < \omega_{pe}$, we have a definite gain over the explicit schemes with the time step $\omega_{pe}\Delta t > 1$ and large grid size $\Delta x \gg \lambda_e$ (the Debye length). Second, due to less complexity of the algorithm, the computational cost per time step with the full-kinetics code is two thirds that with the electron drift-kinetic code. Therefore, large space-scales and a moderate time step make the macro-particle code much more economical than the explicit electromagnetic particle scheme. (A detailed comparison will be made in Section 4).

3. Numerical Methods for the Coupled Equations

3.1 A Key Approximation to the CCFP Equations

To facilitate solution of the coupled field-particle equations derived in Section 2, we need to separate the unknown electromagnetic field from the particle quantities in the summations of Eqs.(26) and (33). For this purpose, we introduce an accuracy-preserving approximation to the CCFP equations,

$$\begin{aligned}\sum_j f_j\tilde{\mathbf{E}}^{n+\alpha}(\mathbf{x}_j)S(\mathbf{x}-\mathbf{x}_j) &= \sum_j f_j\{\alpha(\tilde{\mathbf{E}}^{n+1}(\mathbf{x}_j)-\tilde{\mathbf{E}}_1(\mathbf{x}_j))+\tilde{\mathbf{E}}_0(\mathbf{x}_j)\}\,S(\mathbf{x}-\mathbf{x}_j)\\ &\cong \alpha F(\mathbf{x})(\mathbf{E}^{n+1}(\mathbf{x})-\mathbf{E}_1(\mathbf{x}))+\sum_j f_j\tilde{\mathbf{E}}_0(\mathbf{x}_j)\,S(\mathbf{x}-\mathbf{x}_j),\end{aligned} \tag{37}$$

where $\mathbf{E}_1$ can be any quantity that would well approximate $\mathbf{E}^{n+1}$, $\mathbf{E}_0 = \alpha\mathbf{E}_1+(1-\alpha)\mathbf{E}^n$, and $F(\mathbf{x}) = \sum_j f_j S(\mathbf{x}-\mathbf{x}_j)$. For $\mathbf{E}_1$, we usually use the electric field of the last time step. Note that $(\mathbf{E}^{n+1}-\mathbf{E}_1)$ is paired in Eq.(37) to minimize an error associated with this approximation, and that the tilde has been removed from this term. Using this

prescription, Eqs.(28)-(30) given in Section 2.3(a) are rewritten

$$A(n_i, n_e; \mathbf{B}^{n+1})\ \mathbf{E}^{n+1} \;=\; \mathbf{S}(\mathbf{E}^n, \mathbf{B}^n; \mathbf{B}^{n+1}). \tag{38}$$

Here, the matrix A consists of the vacuum and plasma terms as defined by

$$A \;=\; 1 \;+\; (\alpha c\Delta t)^2(\nabla\nabla - 1\nabla^2) \;+\; D. \tag{39}$$

The plasma dielectric response term is given by

$$\begin{aligned} D^{(DK)} \;=\; & (\alpha\Delta t)^2 \left(\omega_{pi}^2(\mathbf{x})\{1 - \Theta \mathbf{b}^{n+\alpha} \times 1 + \Theta^2(\mathbf{bb})^{n+\alpha}\}/(1+\Theta^2)\right. \\ & \left. + \omega_{pe}^2(\mathbf{x})(\mathbf{bb})^{n+\alpha}\right) \\ & -4\pi(-e)c\alpha\Delta t\ (n_e(\mathbf{x})/B)\ \mathbf{b}^{n+\alpha} \times 1 \end{aligned} \tag{40}$$

for the electron drift-kinetic code, where (**bb**) is a dyadic tensor. For the full-kinetics code, the D matrix is replaced by

$$D^{(FK)} \;=\; (\alpha\Delta t)^2 \sum_{j=i,e} \omega_{pj}^2(\mathbf{x})\{1 - \Theta \mathbf{b}^{n+\alpha} \times 1 + \Theta^2(\mathbf{bb})^{n+\alpha}\}/(1+\Theta^2). \tag{41}$$

The new source vector **S** is now written only by known quantities,

$$\begin{aligned} \mathbf{S} \;=\; & [1 - \alpha(1-\alpha)(c\Delta t)^2(\nabla\nabla - \nabla^2)]\ \mathbf{E}^n + c\Delta t\ \nabla \times \mathbf{B}^n \\ & + D\mathbf{E}_1 \;-\; 4\pi\Delta t\ \{\sum_{j=i} e_i\ [\mathbf{v}_j^n + \alpha\Delta t(e_i/m_i)\left(\tilde{\mathbf{E}}_0 + \frac{\mathbf{v}_j^n}{c} \times \tilde{\mathbf{B}}^{n+\alpha}\right) \\ & /(1+\Theta^2)]\ S(\mathbf{x} - \bar{\mathbf{x}}_j^{n+\alpha}) \;+\; \cdots\cdots \}. \end{aligned} \tag{42}$$

It is extremely important to note with the aforementioned approximation, that a major contribution to the summation $\sum f_j \tilde{\mathbf{E}}^{n+\alpha} S(\mathbf{x} - \mathbf{x}_j)$ is contained in the second term of Eq.(37) for which the "double summation" is taken accurately, well preserving the kinetic flavor of the original equations (first summation for $\tilde{\mathrm{E}}$). The accuracy of this approximation was numerically proved in the previous literature[14] for the thermal eigenmodes in the 2-D magnetized plasma and for the kinetic Alfven wave in the warm (finite temperature) plasma. The present approximation greatly contributes to minimize a degradation of energy conservation. A simpler approximation, *i.e.*, $\sum_j f_j \tilde{\mathbf{E}}^{n+\alpha}(\mathbf{x}_j) S(\mathbf{x} - \mathbf{x}_j) \cong F(\mathbf{x})\mathbf{E}^{n+\alpha}$ results in a rapid and monotonic decrease in the kinetic energy, especially that of the electrons.

3.2 Solution of Nonlinear Implicit Equations

We first notice that the closely-coupled field-particle (CCFP) equations are solved in the real (configuration) space. This is because the coefficients of the CCFP equations are highly space-dependent, thus the convolution of Fourier modes is quite inefficient. Second derivatives in the real space cause a coupling of only three points in one dimension, and 27 or less adjacent grid points in three dimensions.

Following the above argument, we consider the closely-coupled field-particle equations in the form of an implicit matrix equation:

$$A\ \Psi\ =\ S(\Psi). \tag{43}$$

Here, Ψ is an unknown column vector representing the electric field to be solved, A the matrix which includes both the plasma dielectric response and the vacuum term $(\nabla \times \nabla \times)$, and S the source vector. Since the source S depends on Ψ nonlinearly to treat the ponderomotive force, we need to use an iterative method for the solution of the matrix equation (43). First, all the Ψ-linear terms in $S(\Psi)$ are shifted to the left-hand side to treat the equation as implicitly as possible,

$$L\ \Psi\ =\ Q(\Psi). \tag{44}$$

This equation is solved assuming that $Q(\Psi)$ is known to obtain $\Psi^{(+)} = L^{-1}Q(\Psi^{(r)})$. The superscript (r) denotes the last cycle of the iteration. The new value of the (r+1)-th cycle is given in a Newton-Raphson manner, $\Psi^{(r+1)} = \epsilon\ \Psi^{(+)} + (1-\epsilon)\ \Psi^{(r)}$ with $0 < \epsilon \leq 1$. The new value $\Psi^{(r+1)}$ is then back-substituted to $Q(\Psi)$ in the right-hand side of Eq.(44), and the iteration is resumed until convergence. When the Ψ-nonlinearity of Q is not strong, the value $\epsilon = 1$ can be used. However, even when the Ψ-nonlinearity is weak, the back-substitution should be executed once at least and Eq.(44) be solved twice; in the first cycle of the iteration, the unknown $\mathbf{B}^{n+1}$ is replaced by $\mathbf{B}^n$ in Eq.(38).

It is known that an accurate inversion of the matrix L in the core equation (44) is essential to the solution of the nonlinear equation (43). The Gaussian elimination method was successful in one-dimensional simulation as L is a sparse band-matrix.

However, it is unrealistic for a huge matrix in multi-dimensions. A successive over-relaxation method with only the diagonal terms retained in the left-hand side and the new solution back-substituted to the right-hand side of the equation failed eventually due to accumulation of an error.

Alternatively, to obtain an accurate solution of Eq.(44), the recently developed bi-CGSTAB method[21] which iteratively solves unsymmetric linear systems has been introduced. In this iterative method, orthogonality of correction vectors is used to update the solution. The procedure of solving the linear equation, $Ax = b$, is summarized as follows:

For i = 0 : x_0 − an initial guess,

$$r_0 = b - Ax_0,$$

$$\omega_0 = \rho_0 = \alpha = 1,$$

$$v_0 = p_0 = 0.$$

For general i : $\rho_i = (\bar{r}, r_{i-1})$;

$$\beta = (\rho_i/\rho_{i-1})(\alpha/\omega_{i-1});$$

$$p_i = r_{i-1} + \beta(p_{i-1} - \omega_{i-1}v_{i-1});$$

solve $\hat{p}$ from $K\hat{p} = p_i$;

$$v_i = A\hat{p};$$

$$\alpha = \rho_i/(\bar{r}, v_i);$$

$$s = r_{i-1} - \alpha v_i;$$

solve $\hat{s}$ from $K\hat{s} = s$;

$$t = A\hat{s};$$

$$\omega_i = (t, s)/(t, t);$$

$$x_i = x_{i-1} + \alpha\hat{p} + \omega_i\hat{s};$$

$$r_i = s - \omega_i t.$$

Here, K is a pre-conditioning matrix and $\bar{r}$ is arbitrary such that $(\bar{r}, r_0) \neq 0$. The right choice of $\bar{r}$ has a dramatic influence on convergence, but a serious breakdown of the iteration sometimes occurs if the denominators of the coefficients approach zero[21]. For the CCFP equation (38), the bi-CGSTAB method converges generally well for the choice of $\bar{r} = E^n$. Convergence is judged by the residual error $|r_i| \leq \varepsilon|b|$, typically with the

tolerance of $\varepsilon = 10^{-5}$. The pre-conditioning of the matrix A is required to have a good convergence in a small number of iterations. The 3×3 *small matrix* corresponding to the diagonal element $\Psi_{ijk} = (E_x, E_y, E_z)_{ijk}$ should be pre-conditioned simultaneously as a block; the three components of the electric field in Eq.(38) are physically related, or more precisely, the skewed symmetric elements of the small matrix arising from the $\mathbf{E} \times \mathbf{B}$ drift are predominant over the diagonal elements. The accuracy of solution of the CCFP equation (38) has drastically been improved by the bi-CGSTAB method, and its influence on the whole simulation is found to be quite satisfactory.

However, the bi-CGSTAB method occasionally failed in the $\delta\varphi$ equation (35) even with a sophisticated pre-conditioning. This incident known as a wild (non-) convergence occurs abruptly without a specific relation to the physical condition of the plasma. As a cure, the conjugate residual (CR) method has been introduced[22,23]. The CR method uses two (or more) previous correction vectors and imposes orthonormality $(p_i, A^T A p_j) \neq 0$ for $i \neq j$. Its procedure of solving $Ax = b$ is summarized as follows.

$$
\begin{aligned}
\text{For i} = 0: \quad & x_0 \ - \ \text{an initial guess}, \\
& p_0 = r_0 = b - Ax_0, \\
& q_0 = Ap_0, \ \beta_{0,2} = 0.
\end{aligned}
$$

$$
\begin{aligned}
\text{For general i}: \quad & \alpha_i = (r_{i-1}, q_{i-1})/(q_{i-1}, q_{i-1}); \\
& x_i = x_{i-1} + \alpha_i p_{i-1}; \\
& r_i = r_{i-1} - \alpha_i q_{i-1}; \\
& \beta_{i-1,1} = -(Ar_i, q_{i-1})/(q_{i-1}, q_{i-1}), \\
& \beta_{i-1,2} = -(Ar_i, q_{i-2})/(q_{i-2}, q_{i-2}); \\
& p_i = r_i + \beta_{i-1,1} p_{i-1} + \beta_{i-1,2} p_{i-2}; \\
& q_i = Ap_i.
\end{aligned}
$$

An additional use of $s_i = Ar_i$ in the above procedure eliminates one of the two matrix-vector product calculations. The CR method converges rather slowly, as it does linearly with the iterations. But, its convergence is robust since the denominators of the coefficients stay positive definite.

3.3 Normalization

The normalization of physical quantities consists of four basic units, the length: c/ω_{pe}, time: ω_{pe}^{-1}, mass: m_e and electronic charge: e (absolute value). The non-dimensional quantities used in the simulations are,

$$\hat{x} = \frac{x}{c/\omega_{pe}} \ , \ \hat{t} = \omega_{pe} t \ , \ \hat{m}_j = \frac{m_j}{m_e} \ , \ \hat{e}_j = \frac{e_j}{e}. \tag{45}$$

Other quantities such as the velocity, frequency and electromagnetic fields are normalized by combining these basic units:

$$\hat{\mathbf{v}} = \frac{\mathbf{v}}{c}, \ \hat{\omega} = \frac{\omega}{\omega_{pe}}, \ \hat{\mathbf{E}} = \frac{e\mathbf{E}}{m_e c \omega_{pe}} \ , \ \hat{\mathbf{B}} = \frac{e\mathbf{B}}{m_e c \omega_{pe}}. \tag{46}$$

With this normalization, the constant in the field equations is transformed as $(4\pi) \rightarrow (1/n_0)$ and the light speed (c) disappears everywhere (n_0: the average particle number density per unit-length cube).

3.4 Procedures of Parameter Choice

As stated in Section 2, the implicitness parameter α in the equations of motion and the CCFP equations must be in the range $\frac{1}{2} < \alpha \leq 1$. For example, damping rate of the light mode and the Langmuir oscillations are given, respectively, by[14,15] $\omega_i \cong -(\alpha - \frac{1}{2})(ck)^2 \Delta t$ and $\omega_i \cong -\frac{1}{2}(\alpha - \frac{1}{2})\omega_{pe}^2 \Delta t$. Thus the choice of $\alpha > \frac{1}{2}$ damps the light waves and the Langmuir oscillations.

The change in the system energy is also written as the function of the decentering parameter α. The change in the system total energy for the electron drift-kinetic code is defined by

$$\Delta W_{tot} \ = \ \Delta W_F \ + \ \sum_s \Delta W_{K,s}. \tag{47}$$

which is a sum of the change in the electromagnetic field energy and that in the particle kinetic energy. Each term of Eq.(47) is defined by

$$\begin{aligned}
\Delta W_F \ &\equiv \ \frac{1}{4\pi} \int [\mathbf{E}^{n+1/2} \cdot (\mathbf{E}^{n+1} - \mathbf{E}^n) + \mathbf{B}^{n+1/2} \cdot (\mathbf{B}^{n+1} - \mathbf{B}^n)] \, d\mathbf{x} \\
\Delta W_{K,i} \ &\equiv \ \sum_{j=i} m_i \mathbf{v}_j^{n+1/2} \cdot (\mathbf{v}_j^{n+1} - \mathbf{v}_j^n), \\
\Delta W_{K,e} \ &\equiv \ \sum_{j=e} [m_e v_{\|j}^{n+1/2} (v_{\|j}^{n+1} - v_{\|j}^n) + \Delta(\frac{1}{2} m_e v_{\perp j}^2 + \mu_j B)],
\end{aligned} \tag{48}$$

where $\Delta\Psi \equiv \Psi^{n+1} - \Psi^n$. The thermal energy $\frac{1}{2}m_e v_{\perp th}^2 = \mu_j B$ is added to the kinetic energy of the electrons because only the drift motion is included in the guiding-center velocity $\mathbf{v}_\perp$. After some algebra, the change in the system total energy is written[15]

$$\begin{aligned}\Delta W_{tot} \cong & -\frac{c\Delta t}{4\pi}\int \nabla\cdot(\mathbf{E}^{n+\alpha}\times\mathbf{B}^{n+\alpha})\,d\mathbf{x} \\ & -\frac{1}{4\pi}(\alpha-\frac{1}{2})\int[(\mathbf{E}^{n+1}-\mathbf{E}^n)^2+(\mathbf{B}^{n+1}-\mathbf{B}^n)^2]\,d\mathbf{x} \\ & -\Delta t\int \mathbf{E}^{n+\alpha}\cdot(\mathbf{J}^{n+\alpha}-\mathbf{J}_p^{n+1/2})\,d\mathbf{x} \\ & +\sum_{j=e}\frac{1}{2}m_e\{(v_{\perp j}^{n+1})^2-(v_{\perp j}^n)^2\}, \end{aligned} \tag{49}$$

where $\mathbf{J}_p = \mathbf{J}_i + \mathbf{J}_{\|e}$. The second and third terms are negative definite for $\alpha > \frac{1}{2}$ since in the integrand of the third term $\mathbf{J}^{n+\alpha} - \mathbf{J}_p^{n+1/2} \cong (\alpha - \frac{1}{2})\Delta t\,[(e_i^2/m_i)\mathbf{E}^{n+\alpha} + (e^2/m_e)\mathbf{E}_\|^{n+\alpha}]$. The first term of Eq.(49) is the Poynting flux which occurs physically. The second term is the energy loss associated with the numerical damping of the oscillating electromagnetic field. The third term occurs due to imbalance in the joule heating. Therefore, the choice of $\alpha \cong \frac{1}{2}$ is desired to have a good energy conservation, and $\alpha > \frac{1}{2}$ for damping of high-frequency waves. Actually, $\alpha = 0.55 \sim 0.6$ is chosen in the simulations.

For choosing the suitable simulation parameters, it is useful to clarify the restrictions to the present simulation method with respect to the time step and the grid size. First, the time step should be small enough to resolve the cyclotron motion,

$$\omega_{cj}\Delta t \;\le\; 0.2. \tag{50}$$

Even for $\omega_{cj}\Delta t \gg 1$ cases, the "real" particle drifts are recovered[24]. But, the magnetization current which arises from spatial difference in Larmor orbit density is lost for that choice. Secondly, a transit time condition to resolve the structure of the scale length $\lambda = 2\pi/k_{\|,max}$ yields,

$$k_{\|,max}v_\|\Delta t \;\le\; O(0.1), \tag{51}$$

where $v_\|$ is the fastest speed along the magnetic field. The third restriction appears in combination of the time step and the grid size,

$$O(0.1) \;<\; v_\|\Delta t/\Delta x \;\le O(1). \tag{52}$$

The lower inequality arises from an aliasing due to the coarse grid instability[10], and the upper inequality to keep accuracy of the Taylor-expansion in Eq.(33) and that of the predicted particle position $\bar{\mathbf{x}}_j^{n+1/2}$ to evaluate the electromagnetic force.

A slight difference of the predicted particle position $\bar{\mathbf{x}}_j^{n+1/2}$ from the true particle position $\mathbf{x}_j^{n+1/2}$ in the force evaluation may also be a source of numerical heating of the plasma. The difference of the two positions for the electrons, which can be more relevant than the ions because of their large thermal velocity, is written as

$$\delta\mathbf{x}_D \equiv \mathbf{x}_j^{n+1/2} - \bar{\mathbf{x}}_j^{n+1/2} \tag{53}$$

$$\cong (\frac{1}{2}\Delta t)^2 \frac{(-e)}{m_e}(\mathbf{E}_{\parallel}^{n+\alpha} - \mathbf{E}_{\parallel}^{n}) + \frac{1}{2}\Delta t\ (\mathbf{v}_{\perp}^{n+\alpha} - \mathbf{v}_{\perp}^{n}). \tag{54}$$

The restriction may be given in the form of the accuracy condition

$$\frac{|\delta\mathbf{x}_D|}{\Delta x} \cong \frac{\Delta t}{2\Delta x}\,|\{\frac{1}{2}\Delta t\frac{(-e)}{m_e}(\mathbf{E}_{\parallel}^{n+\alpha} - \mathbf{E}_{\parallel}^{n}) + (\mathbf{v}_{\perp}^{n+\alpha} - \mathbf{v}_{\perp}^{n})\}| \ll 1. \tag{55}$$

For a monochromatic sinusoidal wave, $E_{\parallel}^{n} \sim e^{i\omega n\Delta t}$, we have $E_{\parallel}^{n+\alpha} - E_{\parallel}^{n} \approx i\alpha\omega\Delta t\ E_{\parallel}^{n}$. $|\delta\mathbf{x}_D|$ can be made negligibly small compared with the cell size if the value $(v_{th}\Delta t/\Delta x)$ is chosen to be of the order of unity since $\omega\Delta t \ll 1$ for the physically resolved modes $(eE_{\parallel}\Delta t/m_e \leq v_{th})$. However, with too few particles per cell, the deviation due to the fluctuating electric field may be as large as

$$\frac{|\delta\mathbf{x}_{D,n}|}{\Delta x} \approx \frac{\Delta t}{2\Delta x}\,|\{\frac{1}{2}\Delta t\frac{(-e)}{m_e}\,\mathbf{E}_f + \mathbf{v}_{\perp,f}\}|. \tag{56}$$

To make this quantity small compared to unity, one has to choose the time step such that

$$\Delta t\ |(e/m_e)\mathbf{E}_f| \ll v_{th}. \tag{57}$$

The following procedure may be used for the choice of the simulation parameters. We first notice that there are often characteristic spatial scale-lengths in the plasma phenomena such as the wavelength and Larmor radius. The grid size is determined from a resolution requirement. Next, if we specify the magnetic field strength and the electron beta value, the electron thermal speed is determined by

$$\frac{v_e}{c} = \sqrt{\beta_e}\,\frac{\omega_{ce}}{\omega_{pe}}\,. \tag{58}$$

Referring to the conditions Eqs.(51) and (52), the range of allowable time step is determined for the already chosen space-grid size. Here, $\omega_0 \Delta t \ll 1$ must be satisfied with ω_0 the characteristic frequency of the phenomena. The condition Eq.(57) should be kept in mind to reduce artificial heating of the plasma, with which the upper limit of the time step or the minimum number of simulation particles are estimated. Finally, the condition Eq.(50) is referred to in order to determine the lower limit of the mass ratio (m_i/m_e). At this stage, all the parameters may have to be reshuffled to expand their allowable range of variation or to fit the simulation into the given computing resources.

Two remarks are stated concerning modification of the algorithm. First, the identical formula must be applied to the equations of motion and the corresponding parts in the CCFP equations. Second, the same area-weighting scheme should be used both in the evaluation of the electromagnetic field and in the assignment of the particle informations to the space grids[8]. A violation to these rules causes poor momentum and energy conservations and will probably result in numerical instabilities.

4. A Simulation of Collisionless Magnetic Reconnection

Reconnection of magnetic field has attracted much attention as an effective agent of releasing magnetically stored energy to accelerate or heat the space and astrophysical plasmas[25,26]. In magnetic fusion, reconnection causes a drastic topology change in the magnetic surfaces which leads to another stable equilibrium or sometimes loss of plasma confinement. To date, the global study of magnetic reconnection relies on the magnetohydrodynamic (MHD) equations with the Ohm's law which includes ad hoc dissipation of the plasma current ηJ. However, an origin of anomalous resistivity (i.e., dissipation) remains a key question of collisionless reconnection for decades.

A possible role of electron inertia in the collisionless reconnection was first investigated in the MHD framework[27] and was considered in the kinetic viewpoint with the electromagnetic fields being assumed[28]. Later studies focused on the m=1 tearing mode in connection with tokamak sawtooth crash phenomena wherein the MHD (fluid) equations and the generalized Ohm's law with electron inertia current $dJ_{\parallel}/dt$ were adopted[29–32]. Nonlinear growth of magnetic island was studied analytically[33–36] and numerically by particle simulations[37–39].

Nevertheless, the mechanism of collisionless reconnection seems to be still in the mist due to the fluid (MHD) approach. In order to clarify the process from the kinetic standpoint, we study a coalescence of two magnetic flux bundles in the two-dimensional geometry by means of the "macro-particle code" (HIDEN) described in this article. A pair of the same-directional currents in the flux bundles produces both the poloidal and toroidal magnetic fields. The plasma has no externally imposed magnetic field as it often occurs in the solar corona[40]. Thus, a magnetic-null point exists in the present simulation, in contrast to the other particle simulation of collisionless reconnection[7]. Combination of these two studies will make our understanding of collisionless reconnection more complete. It is noted in passing that the coalescence of flux bundles results in the forced reconnection without an external electric field, $E_t^{(0)} = 0$. This makes it easier to identify a generation of the electric field during the collisionless magnetic reconnection.

Because of the presence of the magnetic-null in the plasma, the full-kinetics version of the macro-particle code must be used. To have a better spatial resolution of the so-called "dissipation region" which is characterized by a current sheet to be formed around $x \cong \frac{1}{2}L_x$, spatially-fixed uneven meshes are introduced in the x-direction. Furthermore, to keep the particle fluctuations in a low level, one giant particle is split into a few small particles with the (q_j/m_j) ratio being fixed when it has entered the fine-mesh region. On the other hand, the small particles once split are not coalesced to the original size. A reliable technique would be preferred to artificially coalesce the particles in a two-dimensional domain to reduce the computation time and memory[41].

A charge-neutral plasma is initialized using the same number of ions and electrons (64 ions/cell) which are homogeneously loaded in a doubly-periodic Cartesian system of two dimensions. The system size is $L_x = 400c/\omega_{pe}$ and $L_z = 300c/\omega_{pe}$ with 160×72 cells (the electron inertia length c/ω_{pe} is the unit of length). The grid interval is $\Delta x^{(c)} \cong 1.1c/\omega_{pe}$ for the central part (53 cells) and $\Delta x \cong 3.2c/\omega_{pe}$ for the rest, and $\Delta z \cong 4.1c/\omega_{pe}$ in the z-direction. Three components of the particle velocities are generated according to the Boltzmann distribution of given temperatures. The ions that reside in two square areas are assigned the initial drift $V_{di}/c = 0.01$ in the positive y-direction. All the electrons drift at the same speed initially in the y-direction so that the plasma system has no net dc-current. The maximum strength of the initial poloidal and toroidal magnetic fields are $B_p^{(0)} \cong 0.25$ and $B_t^{(0)} \cong 0.07$, respectively. (The electromagnetic field is normalized like $eE/m_e c\omega_{pe}$.) The physical parameters are the mass ratio $m_i/m_e = 100$, electron thermal speed $v_e/c = 0.2$, and the temperature ratio $T_i/T_e = 1$. The Larmor radius for thermal ions becomes $\rho_i \cong 8c/\omega_{pe}$. The time step is $\omega_{pe}\Delta t = 5$.

Before showing the simulation results, a saving of the computer time with the implicit particle simulation is mentioned. As well-known, the spatial grid size and the time step of the conventional electromagnetic particle-in-cell (EM-PIC) scheme must be the Debye length λ_e and $\omega_{pe}\Delta t \cong 0.2$, respectively. Since $c/\omega_{pe} \cong 7\lambda_e$ in the present run, we need 2800×2100 grids. If we use four ions per cell (minimum) for EM-PIC, it requires 8.0×10^2 times more integration to advance particles for the same physical

time interval. Although the computing time per integration is about three times less for EM-PIC, we need about 270 times more computing time with the conventional particle scheme. For the magnetized electron case[7], the use of $\omega_{pe}\Delta t = 50$ in the implicit particle simulation achieves the gain of two thousand times in the computer time. Moreover, we have to remember that the EM-PIC scheme is subject to exaggerated inter-particle collisions due to high-frequency wave oscillations.

Now, the simulation results are described below. Figure 1 is time snapshots of the poloidal magnetic flux and the ion current at $t/\tau_A = 0$, 1.6 and 3.1. The poloidal flux Ψ is connected with the poloidal magnetic field by $\mathbf{B}_p = \nabla \times (\Psi \hat{y})$. The Alfven time is defined in terms of the initial separation $d = 160c/\omega_{pe}$ of the flux bundle centers and the poloidal Alfven speed $V_{Ap} = B_p^{(0)}/(4\pi m_i n)^{1/2}$, such that $\tau_A = \frac{1}{2}d/V_{Ap}$. In the run, the same-directional currents of the flux bundles attract each other by magnetic force, and the isolated poloidal flux contained in either of the flux bundles begins to merge, starting in Fig.1(b). Reconnection of the magnetic flux is roughly identified by counting the number of the isolated contours in the figure since the poloidal magnetic flux is almost a conserved quantity. A substantial amount of the flux reconnection takes place for $t \geq 1.5\tau_A$. In the lower panels of Fig.1, the ion currents contained in the two square areas first adjust themselves to a more round-shaped profile to have the pressure balance. The centers of the ion currents approach as already seen in the upper panels. But, the merging is not complete, and the contact surface remains rather elongated.

Time development of the y-component of the electric field and current in the gap between the flux bundles is shown in Fig.2 (the signs are reversed). This electric field component, which is purely electromagnetic (no electrostatic part), directly relates to magnetic reconnection via the Faraday's law,

$$\frac{\partial \mathbf{B}_p}{\partial t} \;=\; -c\nabla \times (E_y \hat{y}) \;\neq\; 0. \tag{59}$$

As shown, both the electric field E_y (solid) and the current J_y (dashed) at the x-point undergo an exponential increase with the same growth rate for $t > 0.7\tau_A$, and they saturate around $t = 2.5\tau_A$. We see the proportionality relation, $E_y \propto J_y$, in

the saturation stage. The time history of the isolated poloidal flux $\Delta\Psi$ measured in a macroscopic fashion is shown in the lower panel of Fig.2; the isolated flux $\Delta\Psi$ is defined as the difference of the Ψ values at the flux peaks and the x-point. If we subtract an oscillatory part, a flux merging is observed to be time-linear which begins at $t \sim 1.5\tau_A$. This Sweet-Parker type behavior is the same as the case with the ambient magnetic field[7].

Particle quantities at $t = 1.6\tau_A$ are displayed in Fig.3. The panels correspond to (a) the poloidal (x, z-component) current, (b) the toroidal (y-component) current, (c) the charge density, and (d) the particles that were initially located in the two square regions. The upper panels are for the ions, and the lower panels for the electrons. In the upper panel of Fig.3(a), we can see a distinct poloidal current of the ions toward and off the x-point. The outward current spreads to the full width of the gap sandwiched by the two flux bundles. On the other hand, the electron poloidal current is spatially confined in the narrow channel (dissipation region) where the magnetic field almost vanishes (also see Fig.6). This point sharply differs from the simulation with the ambient magnetic field[7], $B_t^{(0)} \neq 0$. Another remarkable observation in Fig.3 is a generation of the toroidal current of the electrons $J_t^{(e)}$ (panel (b)), which is opposite and stronger than the flux bundle current $J_t^{(i)}$ carried by the ions. The maximum velocity in the y-direction reaches $v_y^{(e)} \sim 4.9 \times 10^{-2} c > V_{Ap}$. The spatial extent of the $J_t^{(e)}$ current is again limited to the narrow dissipation region.

The charge density of Fig.3(c) peaks at the centers of the flux bundles and the dissipation region. This adjustment occurs to maintain the pressure balance; the magnetic field is weaker in these regions. This again differs from the $B_t^{(0)} \neq 0$ simulation. Comparison of $n^{(i)}$ and $n^{(e)}$ shows that the net charge separation is very small. The panels (d) show that the current-carrying ions in either the flux bundles are beginning to meet at the dissipation region. On the other hand, the two populations of the electrons have merged owing to large mobility along the helical magnetic field.

The electric and magnetic fields are shown in Figs.4 and 5 for $t = 1.6\tau_A$ and $2.2\tau_A$, respectively. We first notice that the toroidal component of the electric field E_t in both the figures stays negative in a wide X-shaped region covering the x-point and

extending to the outskirts of the two flux bundles. This negative profile has become apparent early in the run for $t > \tau_A$. However, the poloidal electric field E_p does not have a distinct structure in Fig.4. A converging E_p field appears only after the reconnection has started as seen in Fig.5. (More details will be shown in Fig.6.) The poloidal magnetic field B_p is being compressed in the dissipation region even between the times of the figures. The width of the dissipation region defined by the poloidal magnetic field for $t/\tau_A = 2.2$ is $L_B \cong 3c/\omega_{pe}$ (half-width).

A quadrupole structure is observed in the toroidal magnetic field of Fig.4. This structure arises from the dominance of the poloidal ion current in a large scale as has been shown in Fig.3(a). In the middle of the reconnection process, there appears another small-scale quadrupole structure in the B_t field of Fig.5 which is embedded in the large-scale structure and has opposite signs. This is attributed to that the electron current in Fig.6 is quite concentrated to the narrow channel (dissipation region) and locally supersedes the wide-spread ion current. The electron current profile coincides with the region of weak poloidal magnetic field. This reveals that the incoming electrons into the dissipation region can be ejected only through the narrow unmagnetized channel between the two flux bundles. The maximum outflow speed of the electrons off the dissipation region is $v_p^{(e)} \sim 2.6 \times 10^{-2}c$, which is a few times that of the ions and exceeds the Alfven speed $V_{Ap} \sim 1.8 \times 10^{-2}c$ ($B_p \sim 0.22$ and $n/n_0 \sim 1.5$).

Outside the dissipation region the plasma is magnetized. The current patterns at $t = 2.2\tau_A$ (Fig.6) show that the ions and electrons follow the $E \times B$ drift due to the E_y and B_p fields. In the E_p field of Fig.6, we can see the converging electric field E_x toward the x-line along $x \cong \frac{1}{2}L_x$. This electric field arises from less ion population than that of the electrons in the dissipation region which is due to large Larmor radii of the ions comparable to the dissipation region width. But, it is emphasized that this electric field appears only after the reconnection process has started. Therefore, the charge-separation electric field due to the finite Larmor radius effect plays a secondary role in the collisionless magnetic reconnection.

A few statements should be mentioned about the mechanism of collisionless magnetic reconnection. When the present simulation is compared with the previous one

with the externally imposed toroidal magnetic field[7], it is found that the x-point electric field E_y is generated much in the same way irrespective of the finite Larmor radii of the ions. Figure 7 shows that the quantity that is equal to the displacement current,

$$\frac{\partial E_y}{\partial t} = c(\nabla \times \mathbf{B})_y - 4\pi J_y, \tag{60}$$

becomes negative in the region between the two flux bundles when the growth of the toroidal electric field E_y is observed in Fig.2. This spatial extent is also consistent with the region of the toroidal electric field shown in Fig.4.

However, since the displacement current is a small quantity, the evolution of the toroidal electric field E_y (purely electromagnetic) is actually governed by

$$\nabla^2 E_y \cong \left(\frac{4\pi}{c^2}\right)\frac{\partial J_{Ty}}{\partial t}. \tag{61}$$

In the derivation, $\nabla \times \mathbf{B} \cong (4\pi/c)\mathbf{J}_T$ has been used, where $\mathbf{J}_T$ includes only the divergence-free part of the current $\mathbf{J}$. (This separation is almost impossible except in the Fourier space.) An observed development of the toroidal current,

$$J_y(x,t) = J_0 e^{\gamma t}/\cosh^2(x/L), \tag{62}$$

produces the electric field,

$$E_y(x,t) \cong \left(\frac{4\pi\gamma}{c^2}\right) J_0 L^2 e^{\gamma t} \log\cosh(x/L) + F(t), \tag{63}$$

which agrees with the exponential growth of the toroidal electric field. It can be proved that the response to the electric field is amplified by the plasma compared to the displacement term, i.e., $(\partial J_y/\partial t)/(\partial^2 E_y/\partial t^2) \cong (\omega_{pe}\tau)^2$, where τ is the growth time. This explains the observation in Fig.7. Also, Eqs.(62),(63) are consistent with the observation that the toroidal current is confined in the dissipation region while the toroidal electric field isn't. This is attributed to that the toroidal electric field is not shielded electrostatically where the poloidal magnetic field almost vanishes, and that the electrons are effectively accelerated under such a geometry.

The aforementioned simulation results support the equivalent dissipation to conform with the MHD theory. The x-point electric field E_y accelerates the finite mass electrons

during their transit through the dissipation region. The velocity gain of the electrons will be $\delta v_y^{(e)} \cong ((-e)/m_e)E_y\tau_{tr}$, and the x-point current $J_y^{(e)} \cong (ne^2/m_e)E_y\tau_{tr}$, where τ_{tr} is the electron transit time through the dissipation region. This relation yields the collisionless Ohm's law,

$$E_y \cong \eta_{eq}J_y \tag{64}$$

with the inertia resistivity[28] given by $\eta_{eq} = 4\pi/\omega_{pe}^2\tau_{tr}$. Theoretically, Eq.(64) and the Maxwell equations yield the width of the dissipation region to be $L_B^{(th)} \cong c/\omega_{pe}$.

It is mentioned before making the conclusion that the reconnection rate observed in the implicit particle simulation does change according to the initial magnetic profile. Generally speaking, the reconnection becomes faster when the poloidal magnetic profile is more peaked, and the reconnected flux scales quadratically in time[42], $\Delta\Psi \sim t^2$.

To summarize, the electron inertia effect was confirmed to make collisionless magnetic reconnection possible both in magnetized[7] and unmagnetized plasmas. The finite Larmor radii (FLR) of the ions was found to affect the electron current and cause the quadrupole structure in the toroidal magnetic field. However, the toroidal electric field which directly relates to reconnection was generated independent of the FLR effect, and the FLR effect on the reconnection rate was not observed. A further study is required to know whether this conclusion applies only to the Sweet-Parker regime with $\Delta\Psi \sim t$ or to more general situations.

5. Conclusion

In this article, the algorithm of the closely-coupled implicit method was described which is best applied to the low-frequency, nonlinear kinetic plasma processes. This is because the algorithm filters out high-frequency, small-scale waves, and it makes no intense assumption on the amplitude of the electromagnetic field. Also, the algorithm includes the gyromotion effects, parallel pressure and inertia effects (summarized in Table 1). Numerical methods for the solution of the coupled implicit equations were mentioned in Section 3.

As an application of the algorithm to physics problems, simulation of collisionless magnetic reconnection in the two-dimensional unmagnetized plasma was shown in Section 4, in which the electron inertia was found to play a decisive role. Quantitative comparison of the implicit method and the conventional particle scheme was also made in the section.

Future prospects of the implicit particle method are briefly mentioned. The first issue is an improvement of numerical accuracy which will occur in two folds. One is a use of more sophisticated spatial grids, discretization techniques and matrix inversion method. The other is noise reduction by particle number (size) control by splitting /coalescence procedures, and by introduction of new techniques such as the δf-method which was proven successful in the gyrokinetic scheme[43].

The second issue is to increase the computational ability using massively parallel processors. By domain decomposition of the particle and field quantities, the particle push and summation parts will be rather straightforwardly implemented[44]. However, the method of the field solution differs among the particle schemes. The closely-coupled implicit method currently adopts the bi-CGSTAB and CR methods to invert the matrices of coupled implicit equations. The bi-CGSTAB method involves two matrix-vector multiplications and three scalar-product calculations per iteration cycle. These summations can be taken separately and simultaneously in the processors, and the data transferred among them. With ultra high-speed data link, we will be able to take full advantage of massively parallel processors in the 21-st century.

Acknowledgements

It is an author's pleasure to acknowledge recent collaboration with Dr.J.U.Brackbill on the implicit particle scheme refinement. He thanks Dr.A.Bhattachargee, Dr.J.F.Drake, and Dr.A.Aydemir for discussions about magnetic reconnection and encouragements.

References

1. A.Hasegawa and L.Chen, Phys. Fluids, 19, 1924 (1976).
2. C.Z.Cheng, Phys.Fluids, B3, 2463 (1991).
3. B.Coppi, S.Migliuolo, F.Pegoraro and F.Porcelli, Phys. Fluids, B2, 927 (1990).
4. J.F.Drake and Y.C.Lee, Phys.Fluids, 20, 1341 (1977).
5. B.Coppi, Phys.Rev.Lett., 19, 1207 (1966).
6. M.Tanaka, T.Sato and A.Hasegawa, Phys. Fluids, B1, 325 (1989).
7. M.Tanaka, National Institute for Fusion Science Report No.274; submitted to Phys.Plasmas (1994).
8. C.K.Birdsall and A.B.Langdon, Plasma Physics via Computer Simulation, (McGraw-Hill, 1983).
9. R.J.Mason, J.Comput.Phys., 47, 233 (1981).
10. J.U.Brackbill and D.W.Forslund, J.Comput.Phys., 46, 271 (1982).
11. H.X.Vu and J.U.Brackbill, Comput.Phys.Comm., 69, 253 (1992).
12. A.B.Langdon and D.C.Barnes, Chapter 11 in Multiple Time Scales (Academic Press, 1985).
13. D.W.Hewett and A.B.Langdon, J.Comput.Phys., 72, 121 (1987).
14. M.Tanaka, J.Comput.Phys., 79, 209 (1988).
15. M.Tanaka, J.Comput.Phys., 107, 124 (1993).
16. W.W.Lee, J.Comput.Phys. 72, 243 (1987).
17. J.A.Byers, B.J.Cohen, W.C.Condit, and J.D.Hanson, J.Comput.Phys., 27, 363 (1978).
18. "Hyper-Implicit Decentered Particle Code", or magical skills.
19. A.B.Langdon and B.F.Lasinski, in "Methods in Computational Physics", vol.16, p.327 (Academic Press, 1976).
20. A.B.Langdon, J.Comput.Phys., 30, 202 (1979).
21. H.A. Van der Vorst, Proc. Int'l Symposium on Supercomputing (Fukuoka, Japan (1991)); SIAM J.Sci.Statist.Comput. (1992).

22. P.J.O'Rourke and A.Amsden, Los Alamos National Laboratory Report No.10849 (1986).
23. The use of this method was suggested by Dr.J.U.Brackbill (1992).
24. S.E.Parker, J.Comput.Phys., 97, 91 (1991).
25. J.W.Dungey, Phil.Mag., 44, 725 (1953).
26. J.H.Piddington, Cosmic Electrodynamics (Krieger, 1981).
27. B.Coppi, Phys.Fluids, 8, 2273 (1965).
28. T.W.Speicer, Planet.Space Sci., 18, 613 (1970).
29. J.F.Drake, Phys.Fluids, 21, 1777 (1978).
30. J.F.Drake and R.G.Kleva, Phys.Rev.Lett., 66, 1458 (1991).
31. A.Y.Aydemir, Phys.Fluids, B2, 2135 (1990).
32. J.A.Wesson, JET Report P-27 (1990).
33. D.Biskamp and H.Welter, Phys.Rev.Lett., 44, 1069 (1980).
34. F.L.Waelbroeck, Phys.Fluids, B1, 2372 (1989).
35. X.Wang and A.Bhattacharjee, Phys.Fluids, B4, 1795 (1992).
36. M.Ottaviani and F.Porcelli, Phys.Rev.Lett., 71, 3802 (1993).
37. T.Tajima, F.Brunel and J.Sakai, Astrophys.J., 258, L45 (1982).
38. D.W.Hewett, G.E.Francis and L.E.Max, Phys.Rev.Lett., 61, 893 (1988).
39. M.E.Mandt, R.Denton, and J.F.Drake, submitted to Geophys.Res.Lett. (1993).
40. E.R.Priest, Solar Magnetohydrodynamics (D.Reidel Publ.Co., Holland, 1982).
41. G.Lapenta and J.U.Brackbill, J.Comput.Phys. (to be published).
42. M.Tanaka, in "Theory of Fusion Plasmas" (edited by F.Troyon and E.Sindoni, Societa Italiana di Fisica, 1994).
43. S.E.Parker, and W.W.Lee, Phys.Fluids, B5, 77 (1993).
44. P.C.Liewer and V.K.Decyk and , J.Comput.Phys., 85, 302 (1989).

Table

- Large time-and-space scales: $\omega_{pe}\Delta t \gg 1$, and $\Delta x \geq c/\omega_{pe}$.
- Electromagnetic.
- Multi-dimensions in any geometry (Cartesian, cylinder, torus).
- Inhomogeneous plasma density and magnetic field.
- Kinetic ions; kinetic or drift-kinetic electrons:

$\rightarrow$ { Resonance effects (Landau, cyclotron, bounce resonances)
Orbit effects: Finite Larmor radius effects
Diamagnetic and magnetization effects
Complicated particle trajectories
Electrostatic shielding
Electron inertia – Finite speed relaxation } included.

Table 1. Characteristics of the HIDEN Simulation Code

Figure Captions

Figure 1. The poloidal magnetic flux function Ψ and the toroidal ion current $J_y^{(i)}$ in the upper and lower panels, respectively, for (a) $\omega_{pe}t = 0$, (b) 1.6, and (c) 3.1. The dashed contours correspond to negative values; $\Psi_{max} = 13.6$ and $\Psi_{min} = -9.2$ for the upper panels, and $J_{y,max}^{(i)} = 0.69$ for (a), and $J_{y,max}^{(i)} = 1.5$ for (b) and (c) of lower panels.

Figure 2. Time history of the electric field (solid) and the current (dashed) measured at the x-point in the upper frame, and that of the isolated poloidal flux $\Delta\Psi$ in the lower frame.

Figure 3. (a)(b) The poloidal and toroidal currents, (c) the charge density, and (d) the scatter plot of particles that initially resided in the square regions. The upper panels are for the ions and the lower panels for the electrons at $t = 1.6\tau_A$. The dashed contours correspond to negative values, and the maximum norms are (a) $J_p^{(i)} = 1.0$, $J_p^{(e)} = 1.4$, (b) $J_t^{(i)} = 1.5$, $J_t^{(e)} = 2.6$, and (c) $n^{(i)} = 134$, $n^{(e)} = 135$.

Figure 4. The poloidal and toroidal components of the electric field for $t = 1.6\tau_A$ in the upper panels, and the poloidal and toroidal components of the magnetic field in the lower panels. The dashed contours correspond to negative values, and the maximum norms are $E_p = 3.6 \times 10^{-3}$, $E_t = 1.7 \times 10^{-3}$, $B_p = 0.19$, and $B_t = 7.2 \times 10^{-2}$.

Figure 5. The format is the same as in Fig.4 except that the time is $t = 2.2\tau_A$. The maximum norms are $E_p = 3.8 \times 10^{-3}$, $E_t = 1.4 \times 10^{-3}$, $B_p = 0.20$, and $B_p = 8.3 \times 10^{-2}$.

Figure 6. The magnified plots of the poloidal quantities in the central region around the x-point at $t = 2.2\tau_A$ (the vectors are plotted in every other grid-points in the x-direction). The electric and magnetic fields are displayed in the upper panels, and the ion and electron currents in the lower panels. The maximum norms are $E_p = 4.7 \times 10^{-3}$, $B_p = 0.22$, $J_p^{(i)} = 0.72$, and $J_p^{(e)} = 2.5$.

Figure 7. The y-components of (a) $\nabla \times \mathbf{B}_p$, and (b) $[\nabla \times \mathbf{B}_p - (4\pi/c)\mathbf{J}]$ for $t = 1.3\tau_A$. The dashed contours correspond to negative values.

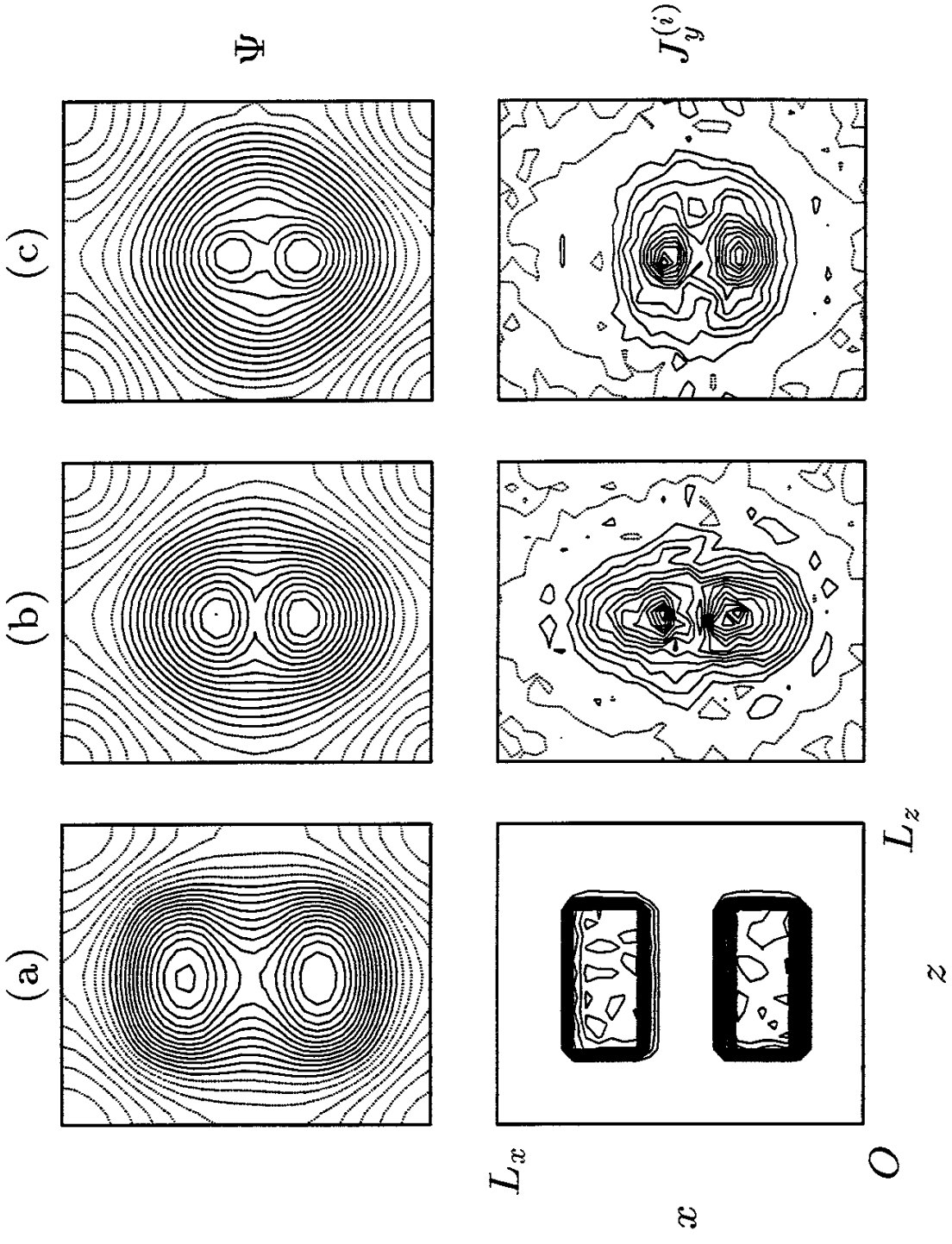

Figure 1.

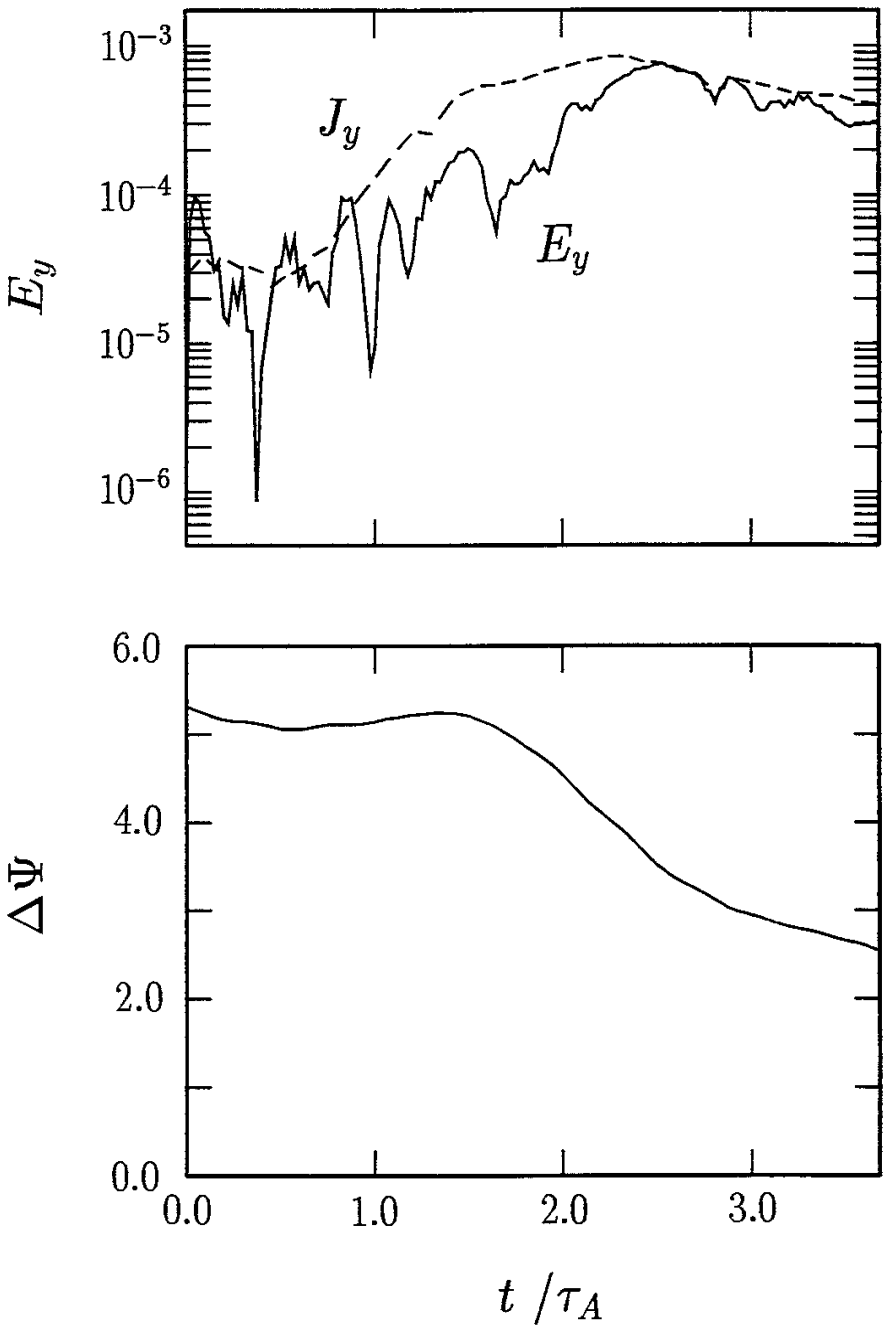

Figure 2.

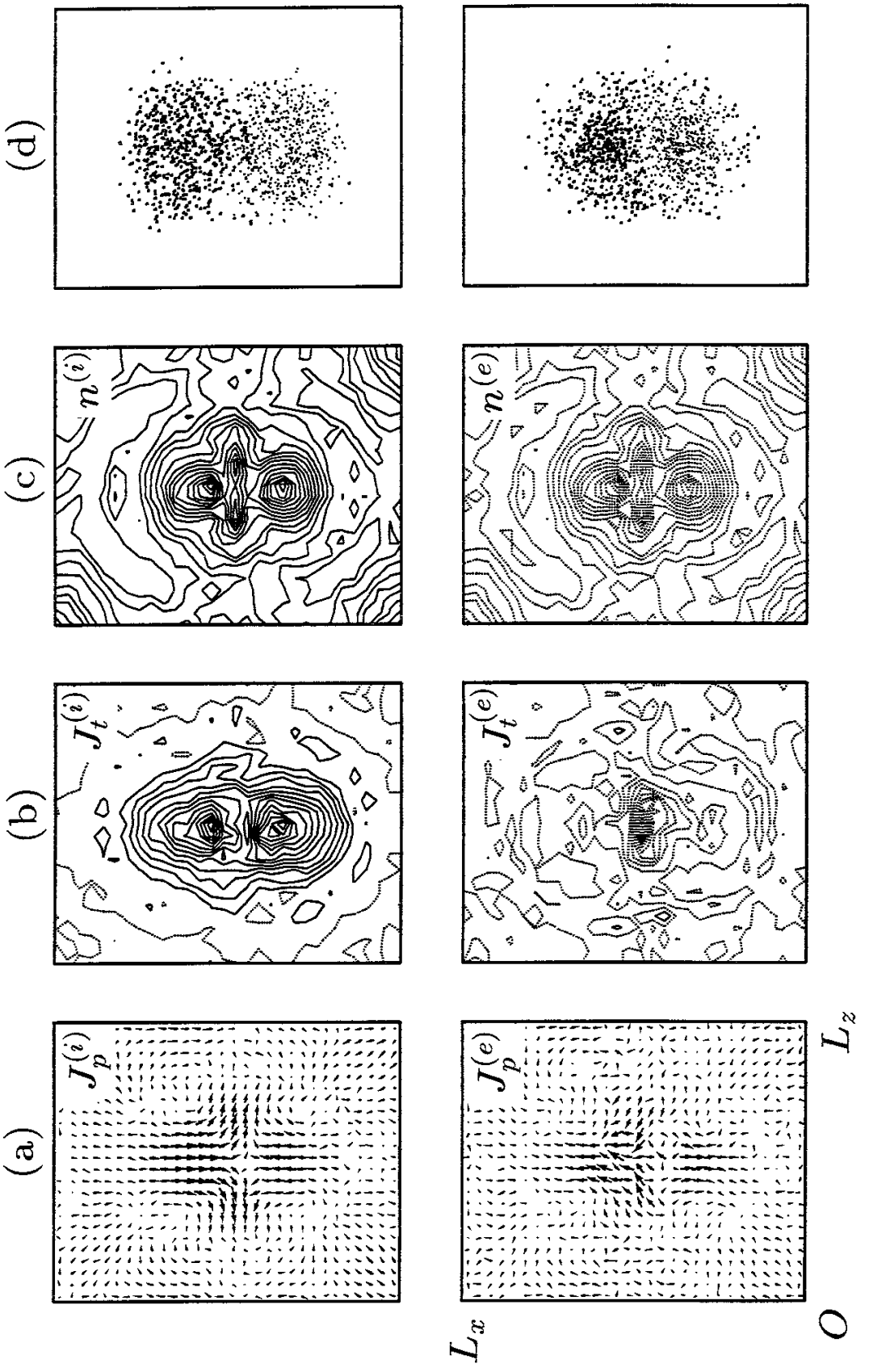

Figure 3.

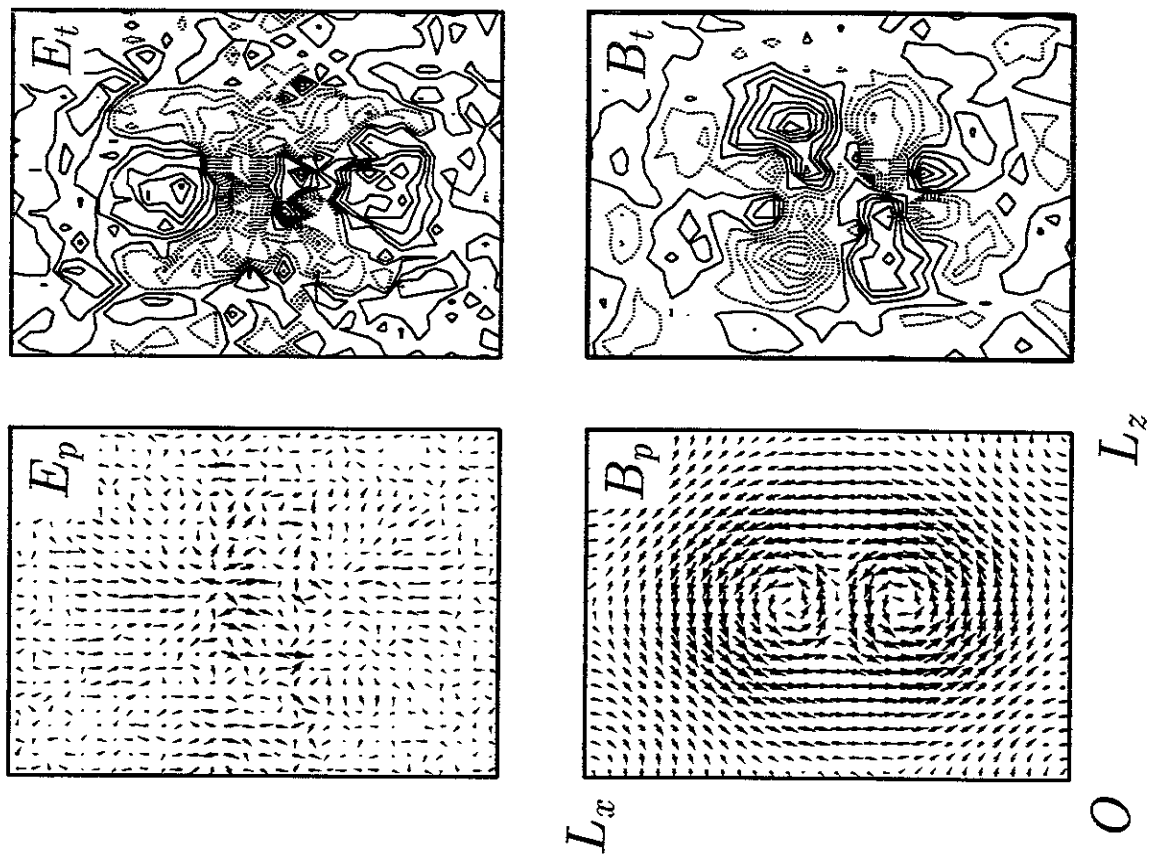

Figure 4.

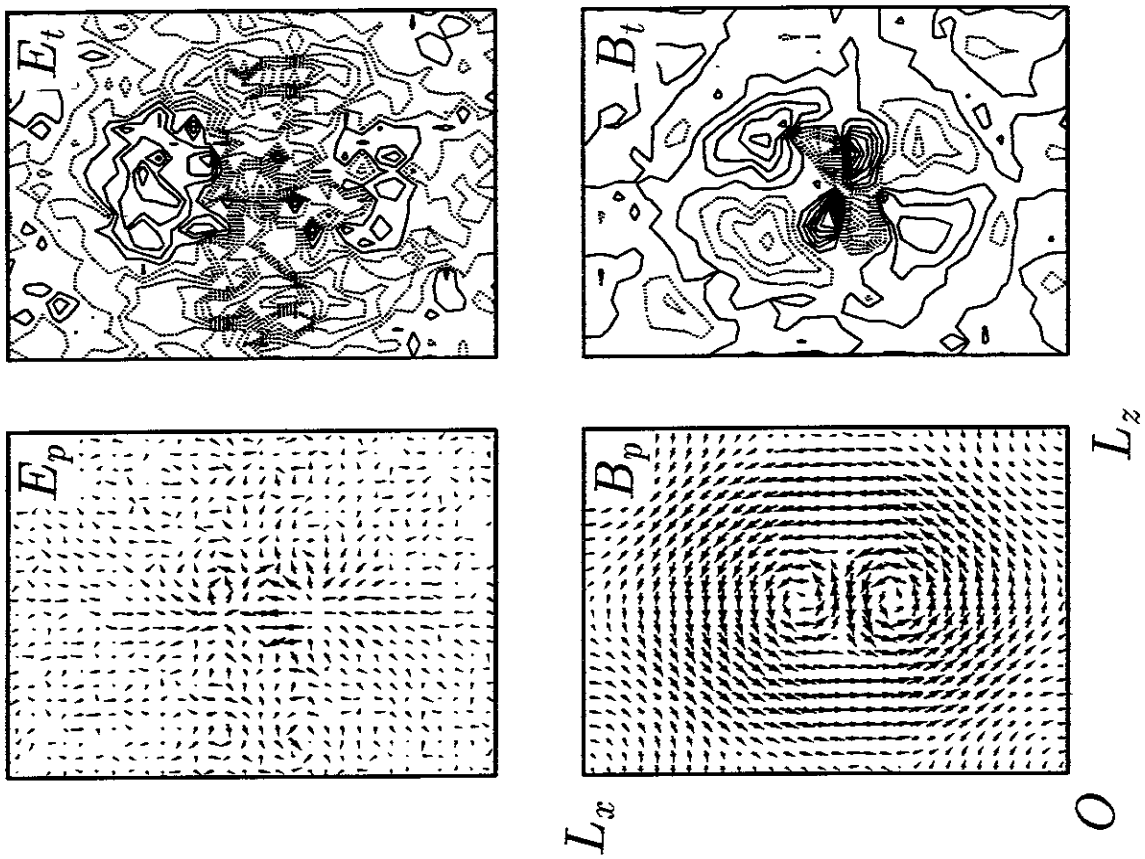

Figure 5.

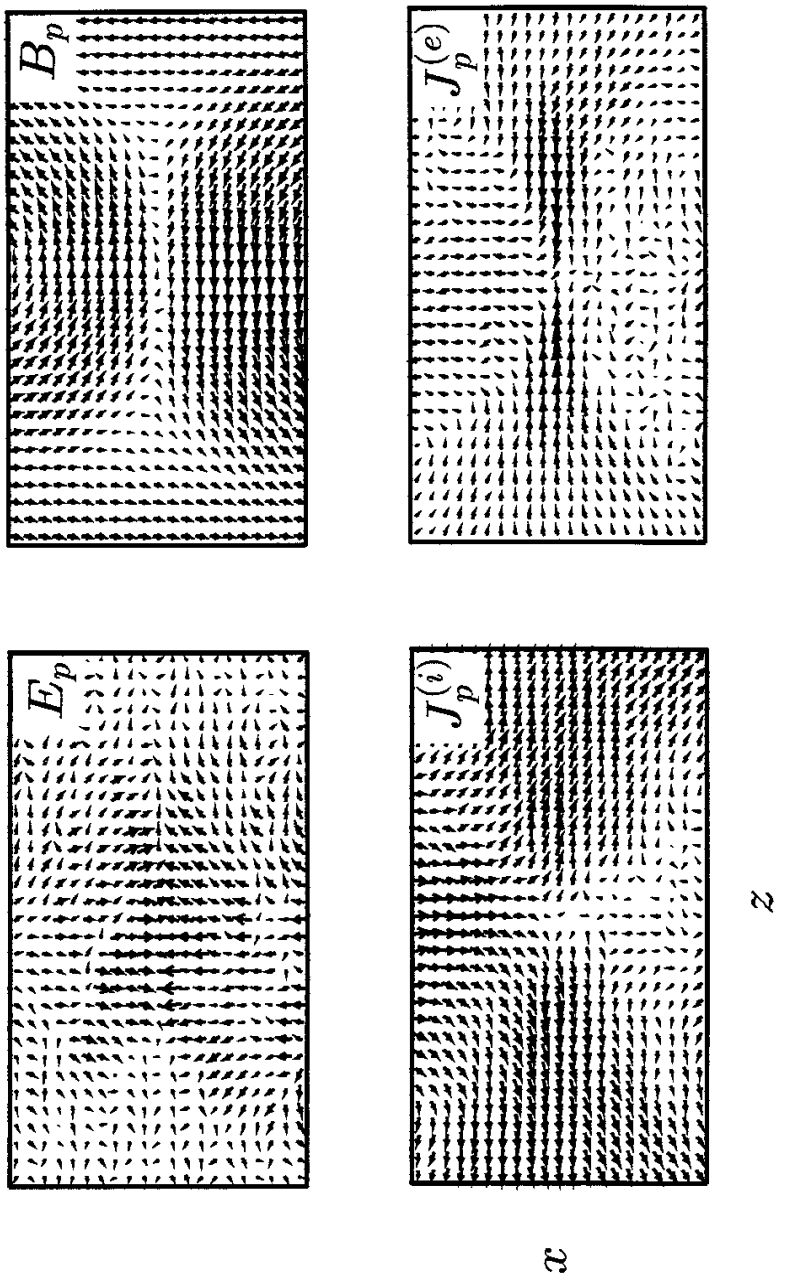

Figure 6.

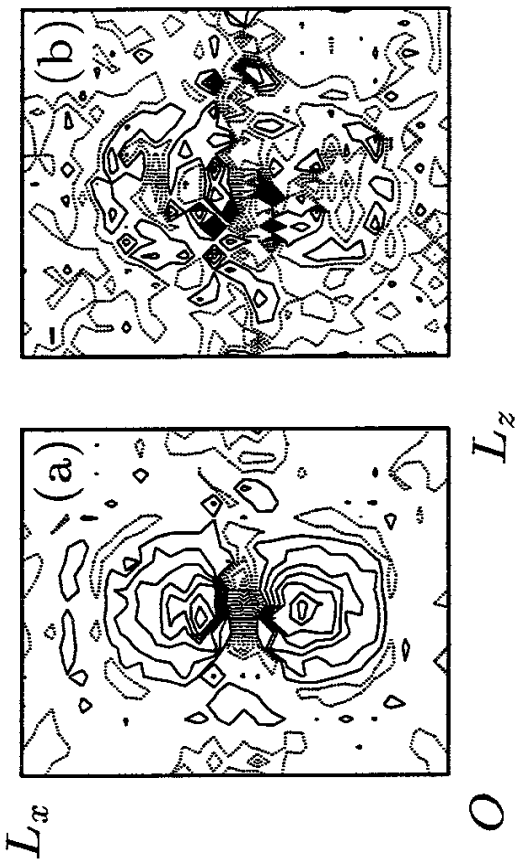

Figure 7.

Recent Issues of NIFS Series

NIFS-278 K. Itoh, S.-I. Itoh, A. Fukuyama, M. Yagi and M. Azumi,
Self-sustained Turbulence and L-mode Confinement in Toroidal Plasmas II; Apr. 1994

NIFS-279 K. Yamazaki and K.Y.Watanabe,
New Modular Heliotron System Compatible with Closed Helical Divertor and Good Plasma Confinement; Apr. 1994

NIFS-280 S. Okamura, K. Matsuoka, K. Nishimura, K. Tsumori, R. Akiyama, S. Sakakibara, H. Yamada, S. Morita, T. Morisaki,. N. Nakajima, K. Tanaka, J. Xu, K. Ida, H. Iguchi, A. Lazaros, T. Ozaki, H. Arimoto, A. Ejiri, M. Fujiwara, H. Idei. O. Kaneko, K. Kawahata, T. Kawamoto, A. Komori, S. Kubo, O. Motojima, V.D. Pustovitov, C. Takahashi, K. Toi and I. Yamada,
High-Beta Discharges with Neutral Beam Injection in CHS; Apr. 1994

NIFS-281 K. Kamada, H. Kinoshita and H. Takahashi,
Anomalous Heat Evolution of Deuteron Implanted Al on Electron Bombardment ; May 1994

NIFS-282 H. Takamaru, T. Sato, K. Watanabe and R. Horiuchi,
Super Ion Acoustic Double Layer; May 1994

NIFS-283 O.Mitarai and S. Sudo
Ignition Characteristics in D-T Helical Reactors; June 1994

NIFS-284 R. Horiuchi and T. Sato,
Particle Simulation Study of Driven Magnetic Reconnection in a Collisionless Plasma; June 1994

NIFS-285 K.Y. Watanabe, N. Nakajima, M. Okamoto, K. Yamazaki, Y. Nakamura, M. Wakatani,
Effect of Collisionality and Radial Electric Field on Bootstrap Current in LHD (Large Helical Device); June 1994

NIFS-286 H. Sanuki, K. Itoh, J. Todoroki, K. Ida, H. Idei, H. Iguchi and H. Yamada,
Theoretical and Experimental Studies on Electric Field and Confinement in Helical Systems; June 1994

NIFS-287 K. Itoh and S-I. Itoh,
Influence of the Wall Material on the H-mode Performance; June 1994

NIFS-288 K. Itoh, A. Fukuyama, S.-I. Itoh, M. Yagi and M. Azumi
Self-Sustained Magnetic Braiding in Toroidal Plasmas: July 1994

NIFS-289 Y. Nejoh,

Relativistic Effects on Large Amplitude Nonlinear Langmuir Waves in a Two-Fluid Plasma; July 1994

NIFS-290 N. Ohyabu, A. Komori, K. Akaishi, N. Inoue, Y. Kubota, A.I. Livshit, N. Noda, A. Sagara, H. Suzuki, T. Watanabe, O. Motojima, M. Fujiwara, A. Iiyoshi,
Innovative Divertor Concepts for LHD; July 1994

NIFS-291 H. Idei, K. Ida, H. Sanuki, S. Kubo, H. Yamada, H. Iguchi, S. Morita, S. Okamura, R. Akiyama, H. Arimoto, K. Matsuoka, K. Nishimura, K. Ohkubo, C. Takahashi, Y. Takita, K. Toi, K. Tsumori and I. Yamada,
Formation of Positive Radial Electric Field by Electron Cyclotron Heating in Compact Helical System; July 1994

NIFS-292 N. Noda, A. Sagara, H. Yamada, Y. Kubota, N. Inoue, K. Akaishi, O. Motojima, K. Iwamoto, M. Hashiba, I. Fujita, T. Hino, T. Yamashina, K. Okazaki, J. Rice, M. Yamage, H. Toyoda and H. Sugai,
Boronization Study for Application to Large Helical Device; July 1994

NIFS-293 Y. Ueda, T. Tanabe, V. Philipps, L. Könen, A. Pospieszczyk, U. Samm, B. Schweer, B. Unterberg, M. Wada, N. Hawkes and N. Noda,
Effects of Impurities Released from High Z Test Limiter on Plasma Performance in TEXTOR; July. 1994

NIFS-294 K. Akaishi, Y. Kubota, K. Ezaki and O. Motojima,
Experimental Study on Scaling Law of Outgassing Rate with A Pumping Parameter, Aug. 1994

NIFS-295 S. Bazdenkov, T. Sato, R. Horiuchi, K. Watanabe
Magnetic Mirror Effect as a Trigger of Collisionless Magnetic Reconnection, Aug. 1994

NIFS-296 K. Itoh, M. Yagi, S.-I. Itoh, A. Fukuyama, H. Sanuki, M. Azumi
Anomalous Transport Theory for Toroidal Helical Plasmas,
Aug. 1994 (IAEA-CN-60/D-III-3)

NIFS-297 J. Yamamoto, O. Motojima, T. Mito, K. Takahata, N. Yanagi, S. Yamada, H. Chikaraishi, S. Imagawa, A. Iwamoto, H. Kaneko, A. Nishimura, S. Satoh, T. Satow, H. Tamura, S. Yamaguchi, K. Yamazaki, M. Fujiwara, A. Iiyoshi and LHD group,
New Evaluation Method of Superconductor Characteristics for Realizing the Large Helical Device; Aug. 1994 (IAEA-CN-60/F-P-3)

NIFS-298 A. Komori, N. Ohyabu, T. Watanabe, H. Suzuki, A. Sagara, N. Noda, K. Akaishi, N. Inoue, Y. Kubota, O Motojima, M. Fujiwara and A. Iiyoshi,
Local Island Divertor Concept for LHD; Aug. 1994 (IAEA-CN-60/F-P-4)

NIFS-299 K. Toi, T. Morisaki, S. Sakakibara, A. Ejiri, H. Yamada, S. Morita, K. Tanaka, N. Nakajima, S. Okamura, H. Iguchi, K. Ida, K. Tsumori,

S. Ohdachi, K. Nishimura, K. Matsuoka, J. Xu, I. Yamada, T. Minami, K. Narihara, R. Akiyama, A. Ando, H. Arimoto, A. Fujisawa, M. Fujiwara, H. Idei, O. Kaneko, K. Kawahata, A. Komori, S. Kubo, R. Kumazawa, T. Ozaki, A. Sagara, C. Takahashi, Y. Takita and T. Watari
Impact of Rotational-Transform Profile Control on Plasma Confinement and Stability in CHS; Aug. 1994 (IAEA-CN-60/A6/C-P-3)

NIFS-300 H. Sugama and W. Horton,
Dynamical Model of Pressure-Gradient-Driven Turbulence and Shear Flow Generation in L-H Transition; Aug. 1994 (IAEA/CN-60/D-P-I-11)

NIFS-301 Y. Hamada, A. Nishizawa, Y. Kawasumi, K.N. Sato, H. Sakakita, R. Liang, K. Kawahata, A. Ejiri, K. Narihara, K. Sato, T. Seki, K. Toi, K. Itoh, H. Iguchi, A. Fujisawa, K. Adachi, S. Hidekuma, S. Hirokura, K. Ida, M. Kojima, J. Koog, R. Kumazawa, H. Kuramoto, T. Minami, I. Negi, S. Ohdachi, M. Sasao, T. Tsuzuki, J. Xu, I. Yamada, T. Watari,
Study of Turbulence and Plasma Potential in JIPP T-IIU Tokamak; Aug. 1994 (IAEA/CN-60/A-2-III-5)

NIFS-302 K. Nishimura, R. Kumazawa, T. Mutoh, T. Watari, T. Seki, A. Ando, S. Masuda, F. Shinpo, S. Murakami, S. Okamura, H. Yamada, K. Matsuoka, S. Morita, T. Ozaki, K. Ida, H. Iguchi, I. Yamada, A. Ejiri, H. Idei, S. Muto, K. Tanaka, J. Xu, R. Akiyama, H. Arimoto, M. Isobe, M. Iwase, O. Kaneko, S. Kubo, T. Kawamoto, A. Lazaros, T. Morisaki, S. Sakakibara, Y. Takita, C. Takahashi and K. Tsumori,
ICRF Heating in CHS; Sep. 1994 (IAEA-CN-60/A-6-I-4)

NIFS-303 S. Okamura, K. Matsuoka, K. Nishimura, K. Tsumori, R. Akiyama, S. Sakakibara, H. Yamada, S. Morita, T. Morisaki, N. Nakajima, K. Tanaka, J. Xu, K. Ida, H. Iguchi, A. Lazaros, T. Ozaki, H. Arimoto, A. Ejiri, M. Fujiwara, H. Idei, A. Iiyoshi, O, Kaneko, K. Kawahata, T. Kawamoto, S. Kubo, T. Kuroda, O. Motojima, V.D. Pustovitov, A. Sagara, C. Takahashi, K. Toi and I. Yamada,
High Beta Experiments in CHS; Sep. 1994 (IAEA-CN-60/A-2-IV-3)

NIFS-304 K. Ida, H. Idei, H. Sanuki, K. Itoh, J. Xu, S. Hidekuma, K. Kondo, A. Sahara, H. Zushi, S.-I. Itoh, A. Fukuyama, K. Adati, R. Akiyama, S. Bessho, A. Ejiri, A. Fujisawa, M. Fujiwara, Y. Hamada, S. Hirokura, H. Iguchi, O. Kaneko, K. Kawahata, Y. Kawasumi, M. Kojima, S. Kubo, H. Kuramoto, A. Lazaros, R. Liang, K. Matsuoka, T. Minami, T. Mizuuchi, T. Morisaki, S. Morita, K. Nagasaki, K. Narihara, K. Nishimura, A. Nishizawa, T. Obiki, H. Okada, S. Okamura, T. Ozaki, S. Sakakibara, H. Sakakita, A. Sagara, F. Sano, M. Sasao, K. Sato, K.N. Sato, T. Saeki, S. Sudo, C. Takahashi, K. Tanaka, K. Tsumori, H.Yamada, I. Yamada, Y. Takita, T. Tuzuki, K. Toi and T. Watari,
Control of Radial Electric Field in Torus Plasma; Sep. 1994
(IAEA-CN-60/A-2-IV-2)

NIFS-305 T. Hayashi, T. Sato, N. Nakajima, K. Ichiguchi, P. Merkel, J. Nührenberg, U. Schwenn, H. Gardner, A. Bhattacharjee and

C.C.Hegna,
Behavior of Magnetic Islands in 3D MHD Equilibria of Helical Devices;
Sep. 1994 (IAEA-CN-60/D-2-II-4)

NIFS-306 S. Murakami, M. Okamoto, N. Nakajima, K.Y. Watanabe, T. Watari, T. Mutoh, R. Kumazawa and T. Seki,
Monte Carlo Simulation for ICRF Heating in Heliotron/Torsatrons;
Sep. 1994 (IAEA-CN-60/D-P-I-14)

NIFS-307 Y. Takeiri, A. Ando, O. Kaneko, Y. Oka, K. Tsumori, R. Akiyama, E. Asano, T. Kawamoto, T. Kuroda, M. Tanaka and H. Kawakami
Development of an Intense Negative Hydrogen Ion Source with a Wide-Range of External Magnetic Filter Field; Sep. 1994

NIFS-308 T. Hayashi, T. Sato, H.J. Gardner and J.D. Meiss,
Evolution of Magnetic Islands in a Heliac; Sep. 1994

NIFS-309 H. Amo, T. Sato and A. Kageyama,
Intermittent Energy Bursts and Recurrent Topological Change of a Twisting Magnetic Flux Tube; Sep.1994

NIFS-310 T. Yamagishi and H. Sanuki,
Effect of Anomalous Plasma Transport on Radial Electric Field in Torsatron/Heliotron; Sep. 1994

NIFS-311 K. Watanabe, T. Sato and Y. Nakayama,
Current-profile Flattening and Hot Core Shift due to the Nonlinear Development of Resistive Kink Mode; Oct. 1994

NIFS-312 M. Salimullah, B. Dasgupta, K. Watanabe and T. Sato,
Modification and Damping of Alfvén Waves in a Magnetized Dusty Plasma; Oct. 1994

NIFS-313 K. Ida, Y. Miura, S -I. Itoh, J.V. Hofmann, A. Fukuyama, S. Hidekuma, H. Sanuki, H. Idei, H. Yamada, H. Iguchi, K. Itoh,
Physical Mechanism Determining the Radial Electric Field and its Radial Structure in a Toroidal Plasma; Oct. 1994

NIFS-314 Shao-ping Zhu, R. Horiuchi, T. Sato and The Complexity Simulation Group,
Non-Taylor Magnetohydrodynamic Self-Organization; Oct. 1994

NIFS-315 M. Tanaka,
Collisionless Magnetic Reconnection Associated with Coalescence of Flux Bundles; Nov. 1994